UNIVERSITA` DEGLI STUDI DI PADOVA
Dipartimento di Ingegneria Industriale

Corso di Laurea Magistrale in Ingegneria Aerospaziale

NUMERICAL INVESTIGATION INTO THE POWER DEPOSITION AND TRANSPORT PHENOMENA IN HELICON PLASMA SOURCES

Relatore

Prof. Daniele Pavarin

Correlatori

Dott. Davide Melazzi

Dott. Marco Manente

Laureando: Mirko Magarotto

Matricola 1065668

Anno Accademico 2014 - 2015

Contents

Abstract

At present high-power (>1kW) Helicon Plasma Thrusters are under development in some projects, as in the Italian SAPERE. Helicon Plasma Thrusters are plasma based propulsive systems in which the plasma is produced and heated in an Helicon plasma source, and then exhausted by means of diverging magnetic field lines. The propulsive figures of merit (e.g. thrust efficiency, specific impulse) are connected to the power deposited into the source. An Helicon plasma source consists on a dielectric cylinder that contains the plasma, a radio frequency antenna that ionizes and heats the plasma, a confining magneto-static field aligned with the axis of the cylinder.

In a Helicon plasma source the power deposition is affected by: antenna-plasma coupling, wave propagation, and plasma transport phenomena. The electromagnetic and plasma dynamics phenomena are studied separately and then coupled in an iterative loop. The ADAMANT code solves for the electromagnetic problem and provides the power deposited into the source; this is the input of a fluid solver that provides the plasma parameters, e.g., plasma density and electron temperature, which in turn are the input of the electromagnetic solver. We have used both a 0-D and a 1-D (radial) fluid solvers to reproduce the plasma response. In the solution of the electro-magnetic problem, a sensibility analysis on the antenna and plasma meshes is necessary in order to accurately represent both the antenna current distribution, and the plasma polarization current, while keeping the computational cost at bay. In coupling ADAMANT with the 1-D fluid solver, the power deposition profile along the radial direction is evaluated by sampling the local deposited power on a structured radial mesh; in regard to the latter case, an analysis on both the unstructured ADAMANT mesh, and the structured radial mesh has been performed to avoid the introduction of numerical noise. Finally, the power deposition profile computed by ADAMANT has been benchmarked against another well-established numerical tool.

We have investigated three different antennas, namely the Single Loop, the Nagoya type III, the Fractional Helix. The input parameters investigated in this study are: (i) the magneto-static field from 250 G to 1000 G; (ii) the initial neutral background pressure from 1 mTorr to 30 mTorr; (iii) the voltage that drives the antenna in the range from 100 V to 500 V. Our numerical tools evaluate the following parameters at the equilibrium of the discharge: the plasma density, the electron temperature, the neutral pressure, and the power absorbed by the source. We have found that the power deposited into the source strongly depends on the magneto-static field, and the voltage, whereas the neutral background pressure has a weaker effect. In particular, there is a linear relation between the equilibrium plasma density and the power transferred into the source. The solution of the transport with the 1-D fluid solver has evidenced a peak of the deposited power profile near the edge of the discharge, where the density decreases, while the electron temperature is approximately constant along the radial direction. Finally, there is a good agreement between the 0-D and the 1-D fluid models. As far as the antenna is concerned, the equilibrium parameters depend on the antenna configuration, while the current distribution thereon depends on the plasma density. No antenna performs the best in the range of parameters considered.

List of Symbols

$\mathbf{E}$	electric field	[V/m]
$\mathbf{D}$	electric flux density	[C/m^2]
$\mathbf{B}$	magnetic induction	[T]
$\mathbf{H}$	magnetic field	[A/m]
$\mathbf{J}$	electric current density	[A/m^2]
ϕ	electric potential	[V]
ρ	volume charge density	[C/m^3]
q	charge	[C]
$\mathbf{v}$	particle velocity	[m/s]
m	azimuthal mode number	
k_z	axial mode number	
L	device length	[m]
f	frequency	[Hz]
ω	angular frequency	[rad/s]
ϵ_0	free space electric permittivity	[F/m]
μ_0	free space magnetic permeability	[H/m]
ϵ	electric permittivity	[F/m]
μ	magnetic permeability	[H/m]
c	speed of light in vacuum	[m/s]
χ	electric susceptibility	
χ_m	magnetic susceptibility	
M	magnetization	[A/m]
$\mathbf{k}$	wave vector	[rad/m]
δ	phase	[rad]
v_ϕ	phase velocity	[m/s]
v_g	group velocity	[m/s]
k_0	free space wavenumber	[rad/m]
λ_0	free space wavelength	[m]
n	plasma density	[m^{-3}]
T_e	electron temperature	[eV]
p_n	neutral pressure	[mTorr]
p_{n0}	initial neutral pressure	[mTorr]
B_0	quasi-axial magneto-static field	[G]
ΔV	antenna voltage	[V]
Pw	deposited power	[W]
Pw_r	radial deposited power	[W/m^2]

List of Acronyms

RF	Radio Frequency
H	Helicon
TG	Trivelpiece-Gould
EM	ElectroMagnetic
FDFD	Finite-Difference Frequency-Domain
FDTD	Finite-Difference Time-Domain
HPT	Helicon Plasma Thruster
MoM	Method of Moments
PEC	Perfect Electric Conductor
SWG	Schaubert-Wilton-Glisson
RWG	Rao-Wilton-Glisson

Chapter 1

Introduction

1.1 The Helicon Plasma Source

An Helicon plasma source (Fig.1.1) is a device for the production of a plasma discharge. We can consider this source composed of four parts: (i) a neutral gas source, (ii) a dielectric cylinder for the confinement of the plasma, (iii) a RF antenna, (iv) coils for the production of a quasi-axial magnetostatic field. The plasma is produced ionizing a neutral gas stored in a pressured tank. The dielectric cylinder is necessary for the confinement of both the plasma and the residual neutral gas, in fact in those sources only weakly ionized plasma is produced. The RF antenna is the mean that drives the discharge. The coils generate a quasi-axial magnetostatic field, usually < 0.15 T, it is required both for the confinement of the plasma and for the propagation of whistler waves[1]. The propagation of those waves is possible if and only if the quasi-axial magnetostatic field is present [1], and the mechanism of power deposition that involves those waves has an high efficiency [2]. The employment and the study of this technology are mainly due to the low amount of power (the highest being 3.2 kW for Beal and Mak's antenna [3], 1.2 kW for Pucci's antenna [4]) required to achieve high values of plasma density (e.g. 10^{19} m^{-3}), thus making this system very efficient. It is possible to generate high-density plasma, up to 10^{19} m^{-3}, with a weak magnetic field, < 0.1 T, and a simple antenna geometry [5], [6].

The first experiments on gaseous plasma were conducted in 1960 on a toroidal geometry, with probe like transmitting and receiving antennas [7]. Blevin and Thonemann [8] used in their experiments a cylindrical plasma column with a quasi-axial magnetic field of 200 mT and the antenna frequency varying between 6-28 MHz. Lehane and Thonemann's experiment [9] was the first to study the wave propagation inside an Helicon plasma sources. In this experiment the shape of the plasma container was cylindrical, the magnetic field B0 < 50 mT, 3 kW of generated power for the antenna and the pressure of the Xenon gas in the range 10-70 mTorr. In the late 60's, in Australia, Boswell used a small diameter glass tube for physical confinement of the plasma, along with a double loop antenna [10]. Still today there are many kinds of antennas used in Helicon plasma sources: from the single-loop antenna, or Stix coil [11], to the helical antenna [12]. Only in 1978 the Nagoya type-III geometry was studied [13], as a simplification of a double-loop antenna. In the early 80's, the Helicon source has been employed also to simulate atmospheric plasma [14]. But, with the emerging computer industry in the same years, the primary field of application of the Helicon plasma sources has become the semiconductor processing, which includes etching and deposition of integrated circuits. Other uses comprise of electrodeless beam sources, laser accelerators and plasma thrusters [15]. In the years following the first use of the Nagoya type-III antenna, the Helicon source system has remained the same with some minor changes, whereas the studies in this period were more focused on the physics of wave propagation and the mechanism leading to power deposition in such plasma sources.

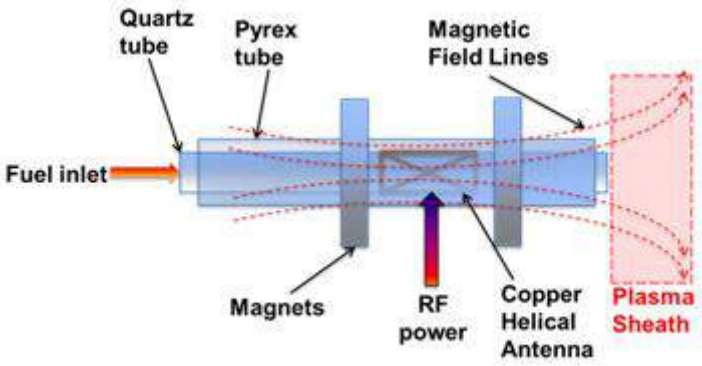

Figure 1.1: Helicon plasma source

1.2 Major Theoretical Findings

The processes that occur in a Helicon plasma source, and affect the power deposition are: antenna-plasma coupling, wave propagation, and plasma transport. The physics behind these processes is to be grasped in order to perform the design and possibly optimization of such a plasma source. Standard approaches rely on electromagnetic simulations coupled to either fluid or or kinetic or Particle-In-Cell (PIC) strategies to reproduce the plasma response.

1.2.1 Electro-Magnetic

The electromagnetic study of Helicon sources can be divided primarily in two parts: antenna-plasma coupling and propagation of the whistler waves. The whistler waves are produced by the RF antenna, they propagate within the plasma cylinder and are responsible of the power deposition. These whistler waves are characterized by the frequencies ω where, $\omega_{LH} \ll \omega \ll \omega_{ce} \ll \omega_{pe}$, the first is the lower hybrid frequency, the last are the electron cyclotron frequency and the plasma frequency.
The theoretic study of wave propagation has been mainly conducted starting from the dispersion relation that arises from Maxwell wave equations used to study electromagnetic waves within a plasma medium. In the early years, with the use of the simplification hypothesis $m_i \gg m_e$, it was thought that only the fast wave (i.e. Helicon wave) propagates within the plasma in an Helicon source. But with more accurate experimental investigations it was noticed a discrepancy, close to the boundary of the plasma cylinder [16], in respect to the simulations. Already in 1959 Trivelpiece and Gould [17] (from whom the waves get their name) proposed the idea of a second wave coupled to the Helicon but only at the end of '90s F.F.Chen and D.Arnush published some works [1],[18],[19] in order to sumarize the theoretical and experimental results obtained until then on the electromagnetic waves propagation in an Helicon plasma source. The coherent formulation of those results takes the name of Helicon theory. In the limit of small amplitude waves we can assume an harmonic dependance to time and space in the form of $\exp j(m\theta + kz - \omega t)$ for fields and sources, so the dispersion relation reads

$$\delta \nabla \times \nabla \times \mathbf{B} - k \nabla \times \mathbf{B} + k_w^2 \mathbf{B} = \mathbf{0} \tag{1.1}$$

where $\delta = (\omega + j\nu)/\omega_{ce}$, ν is a factor that takes into account the plasma collisionality, $k_w^2 = \delta(\omega_{pe}/c)^2$, and c the speed of light in vacuum. Eq.1.1 has two solutions: the H wave and the TG wave. Their total wave numbers can be expressed as

$$\beta_{1,2} = \begin{cases} \frac{k_w^2}{k} & for \;\; H \\ \\ \frac{k}{\delta} & for \;\; TG \end{cases} \tag{1.2}$$

The power deposition is related to two phenomena chiefly: the plasma collisionality and the Landau dumping. The first is related to the energy dissipation because of the collisions between charged particles and charged-neutral particles, the second is connected to the energy that waves transfer to electrons. The hypothesis that Landau damping was predominant in the power deposition was first introduced by F.F. Chen in 1991 [20] (before the discovery that TG waves play a fundamental role in the power deposition). As the studies on TG waves progressed, Landau damping became a less effective phenomenon involved in the power deposition in Helicon discharges. It was only in 1998, after the discovery of TG waves and further studies, that it was confirmed that Landau damping is not a predominant cause for power deposition in Helicon sources [21].

Parallel to physical models there was a development of numerical codes to better understand the physics behind a Helicon plasma source. The first study containing a computer code, "ANTENA", conceived for Helicon plasma sources goes back to 1996. This code is able to compute the radial profiles, the power deposited and the antenna impedance [2]. Several numerical approaches have been followed in the years to better understand some specific aspects of the plasma behavior. For instance to investigate density profile effects of Helicon plasmas, Mouzouris and Scharer developed the ANTENA2 simulation code [22]. Here the EM fields are decomposed into transverse electric and transverse magnetic waveguide modes. Another approach was adopted by Chen and Arnush in the HELIC code [1,18,23]. It is based on the numerical integration of a fourth-order ordinary differential equation by means of a numerical boundary-value problem. In 2012 Melazzi *et. al*, developed the code SPIREs (plaSma Padova Inhomogeneous Radial Electromagnetic solver), a FDFD electromagnetic solver in one dimension for the rapid calculation of the electromagnetic fields and the deposited power in a cylindrical plasma problems [24]. The Maxwell wave equations are discretized with a constructed mesh along the radial direction of the cylinder, and Fourier transformed along the other two dimensions and in time. The plasma can be inhomogeneous, finite-temperature, collisional, magnetized and multi-species. Most of the approaches followed in the last years involved simple geometric antennas modeled with the thin-wire approximation (the induced current density is assumed rather than computed). Those models cannot provide accurate information on the current distribution, the radiated fields and the antenna impedance. In 2014 Melazzi and Lancellotti developed the code ADAMANT (Advanced coDe for Anisotropic Media and ANTennas), designed to study antenna geometries and their influence in power deposition in a Helicon plasma source [25].

1.2.2 Particle In Cell

In a PIC [26,27,28,29,30] simulation the plasma dynamics is modeled by means of an iterative loop (see Fig.1.2): (i) the electromagnetic fields are calculated from the position and the velocity of the particles that compound the system, (ii) the particle motion is calculated once the electromagnetic field are known. In a run there can be thousands of iterations, because the time step of the simulation depends on the characteristic times of the phenomena that drives the plasma motion, e.g. the period of the plasma oscillation. Therefore the PIC approach cannot be implemented solving the equation of motion for each particle, since the related computational cost is too high. The classical way in which a PIC simulation is implemented in a numerical solver is based on the introduction of *clouds* of particles. This means dividing the real particles in a finite number of groups where each particle is supposed to have the same properties (e.g. the same specie, the same velocity). In other words at

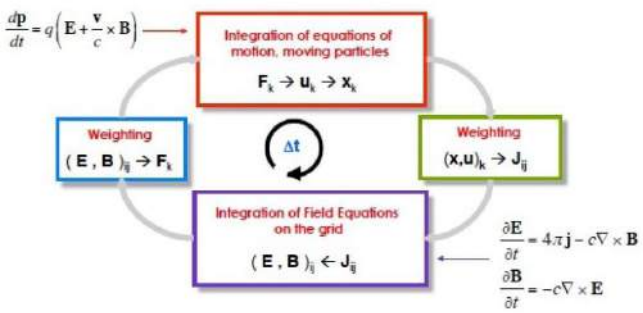

Figure 1.2: Iterative loop in a PIC simulation

each group of real particles is associated one particle (called computational particle) that describes the motion of the group. The number of real particles that compound a *cloud* cannot be to high otherwise the physics of the problem are coarsely simulated (e.g. the gradients of current density, and therefore of the EM field); reversely the number of the *clouds* cannot be huge because of the increasing computational cost. Thence in a PIC simulation it is necessary to find a trade-off between those two instances; however if the plasma density is higher than a threshold value (approximately 10^{19} m^{-3}) it is difficult to combine physical accuracy with a reasonable calculation time.

The trajectories of the computational particles, in the phase space, are calculated in a lagrangian reference frame, instead of the electromagnetic fields that are calculated in a space grid (so the PIC method is an hybrid formulation lagrangin-eulerian). It is worthwhile to underline that the computational particle describes the motion of a group of real particles, occupying a finite region of space.

1.2.3 Fluid

The majority of plasma phenomena observed in real experiments can be explained considering the plasma as a fluid: the identity of each single particles is neglected because it is assumed that the particles move statistically together. In an ordinary fluid this assumption relies on the huge amount of collisions between particles. However it can be proved that it is sufficient that the random thermal velocity is the same of a Maxwellian distribution so that the momentum fluid equation can describe the plasma motion [31]. It is not required a Mawellian distribution, usually associated to high collisionality, to apply a fluid model. Another reason because the fluid model works is the presence of magnetic fields; the gyration motion plays an effect similar to collisionality in respect to the particle motion, especially in the direction perpendicular to the force lines [31].

The major simplicity in theoretical models and the minor computational cost in numerical simulation make the fluid model more suitable to reproduce the plasma motion than kinetic or PIC models in many practical cases. To calculate the equilibrium conditions of RF heated plasma sources it is necessary to solve the two coupled problems of the electromagnetic power deposition and the macroscopic transport of charged and neutral species. In 2012 Curreli, Melazzi, *et al.* developed a numerical tool conceived to quickly calculate the radial equilibrium conditions in an cylindrical Helicon plasma source [32]. The SPIREs [25] code

provides the input source terms for the transport problem. The continuity and momentum equations of a single-ionized cold plasma, together with energy conservation, have been solved along the radial direction by the EQM code, whose fluid model relies on a non-classical theory proposed for the evaluation of the equilibrium conditions of plasma cylinders of finite-length [33].

Another work in which it was studied the equilibrium of a RF heated plasma sources go back to 2003. Bose, Govindan, Meyyappan modeled an axisymmetric Helicon plasma source through 2-D plasma fluid equations and wave equations [34]. In order to solve the plasma transport and the wave equations it was used the semiconductor equipment modeling software (SEMS) developed at the NASA Ames Research Center [35]. SEMS uses a finite-difference method to solve a system of partial differential equations using a fully coupled implicit scheme. The wave equations are solved in the discharge and the vacuum space all the way to the inner electromagnet surface. A self-consistency between the plasma transport and wave equations is obtained by exchanging information between the two modules after every time step. The RF plasma power profile is obtained from the wave amplitudes to be used in momentum equations. Similarly, the wave equations use an updated conductivity matrix after every time step of the momentum equations.

1.3 Helicon Sources in Space Propulsion

Recently, plasma-based propulsion systems are beginning to challenge the monopole of chemical thruster in space applications. The high specific impulse, which allows for a huge reduction in the propellant mass, and high thrust efficiency make the plasma thruster an attractive solution for space propulsion. Whereas in a chemical rocket, the specific impulse is an intrinsic characteristic related to the propellant calorific energy per unit of mass, in plasma propulsion systems, the specific impulse is extrinsic, depending on the electromagnetic energy deposited into the plasma. The propulsive figures of merit, such as specific impulse, exhaust velocity, and thrust efficiency are related to the plasma parameters, i.e. gas type, neutral pressure, magneto-static field, plasma density and temperature, that in turn are related to the power transferred to the plasma and the plasma transport. Recent advances in plasma-based propulsion systems have led to the development of electromagnetic RF plasma generation and acceleration systems, called HPT. Many plasma-based propulsion systems, today at the state of the art e.g. ion engines and Hall-effect thrusters, have proven to have high efficiencies in plasma generation, though they have critical issues:

- their lifetimes are limited by the erosion of the extracting grids and the ceramic walls,
- they need an external cathode for charge compensation,
- they exhibit low power density.

Reversely, the HPTs are characterized by a long life (electrodes or neutralizers are not necessary in those thrusters) and an high power density. This is the reason why in the last years the interest in the space propulsion applications of the Helicon sources is growing up, even thought their primary field of application remains the semiconductor processing.

In Fig.1.3 are sketched the three main systems involved in a HPT: a gas feeding system, an Helicon plasma source, electromagnetic diverging nozzle. The feeding system injects a neutral gas into the dielectric cylindrical chamber, here a RF antenna produces the ionization as usually happens in an Helicon source. The magnetic coils provide the quasi-axial magnetic field necessary for both the propagation of whistler waves and for the confinement of the plasma. At the exhaust section the force lines become divergent providing a "magnetic nozzle" effect on the plasma, thus allows the detachment of the charged particles from the nozzle and so the generation of the thrust. Specifically the plasma is exhausted by means of fluid-dynamics and electro-magnetic processes, which lead to the supersonic acceleration of plasma and the consecutive detachment from the magnetic nozzle [37].

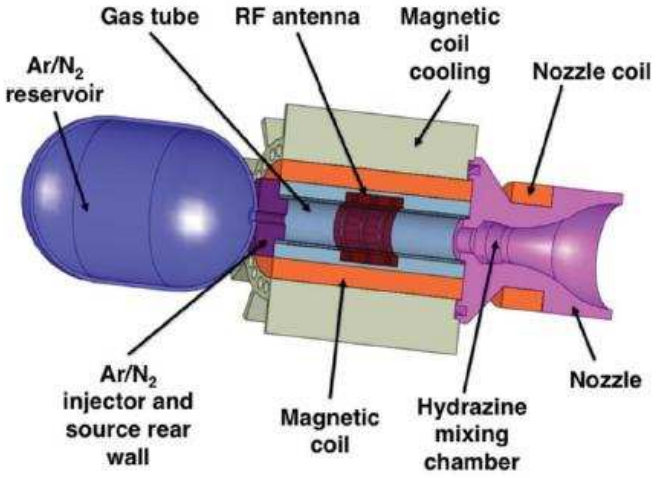

Figure 1.3: Helicon Plasma Thruster developed in the HPH.COM project [36]

Two projects that have been developing the technology of the HPT are the European HPH.COM (Helicon Plasma Hydrazine Combined Micro)[38][39], and the Italian SAPERE (Space Advanced Project for Excellence in Research and Enterprise)[40]. In HPH.COM, a compact low-power (in the range of 50 W) plasma thruster using high efficiency RF sources was developed for attitude and position control of mini-satellites. The design of the thruster was pursued with a synergic theoretical and experimental approach, also thanks to the development of innovative electromagnetic and plasma codes. An high-power ($>$ 1 kW) plasma thruster is under development in the project SAPERE. The consortium for the design and realization of SAPERE is led by Thales Alenia Space Italia and involves also CISAS as one of the major partner. SAPERE is organized in two sub-projects STRONG and SAFE. SAPERE/STRONG aims at the realization of a reusable space tug coupled to the rocket VEGA for the transfer of payloads of different sizes from an intermediate orbit to the target orbit; SAPERE/SAFE has as its primary purpose the improvement of services for emergency management (crisis management) in different domains, with a wider use of space technology in order to improve the possibility of observing from space, to communicate with space infrastructure, or to know the precise location. The electric propulsion system will be a HPT with an input power $>$1 kW; the design of this very thruster will be based on the scaling up of the prototype developed during the project HPH.COM.

In the SAPERE/STRONG project, a high-power Helicon source will be designed and developed; this source is expected to attain high values of plasma density, i.e. in the order of 10^{19} m^{-3}. Such high values of the plasma density are not achievable by PIC method, and would result in long simulation time and huge computational costs in a kinetic approach.

To model the coupling of the wave propagation and the plasma transport in such a source it is possible to study separately the electromagnetic and plasma dynamics phenomena. These phenomena will be solved by means of an electromagnetic and a fluid solver, respectively, whereas both solvers will be coupled through an iterative loop. In this loop the output of the electromagnetic solver (the power deposited into the plasma) is the input of the fluid solver that solves for the plasma transport. Similarly, the output quantities of the fluid solver, e.g. plasma density and electron temperature, are the input for the electromagnetic solver. These two tools will iterate until convergence criteria are satisfied. In this work, the ADAMANT code will solve for the electromagnetic coupling between the antenna and the plasma discharge. Two fluid solvers will be used, namely:

- a zero-dimensional model, dubbed Global-Model and developed during the HPH.COM project, that solves for the uniform values of the plasma density, electron temperature, and neutral pressure within the discharge;
- a one-dimensional model that solves for the radial profiles of the plasma density, electron temperature and neutral pressure.

Both fluid solvers will be coupled to ADAMANT, and the resulting numerical tools will be benchmarked against others well-established tools.

Chapter 2

ADAMANT numerical code

This chapter aims at giving an introduction to the solver ADAMANT, a quick explanation of its principles and a brief user guide will be produced. ADAMANT is a full-wave numerical tool developed for the study of wave propagation and for the design and optimization of antennas in Helicon plasma sources. ADAMANT relies on a set of coupled surface and volume integral equations, the unknowns are the surface electric current density on the antenna and the volume polarization current in the plasma. The latter can be inhomogeneous and anisotropic whereas the antenna can have arbitrary shape. The set of integral equations is solved numerically through the Method of Moments (MoM) [41]in the form of Galerkin. This approach allows the accurate analysis of the antenna and the antenna-plasma coupling.

2.1 Problem Formulation

In ADAMANT the EM model of an Helicon Plasma Source consists in (i) the plasma volume(s) V_P , and (ii) the metallic part(s) S_A, which are immersed in a background medium. The metallic parts (e.g. the antenna) are considered 2D because of the skin effect.

The EM response of the V_P is modeled through a set of polarization currents, which result non-null only in the plasma region

$$\mathbf{J_P} = j\omega(\mathbf{I} - {\epsilon_\mathbf{r}}^{-1}) \cdot \mathbf{D_P} \tag{2.1}$$

The tensors $\epsilon_\mathbf{r}$ denote the plasma permittivity relative to free space. In a system of cartesian coordinates where $\mathbf{B_0} = B_0\hat{\mathbf{z}}$ the relative permittivity of the plasma is

$$\epsilon_\mathbf{r} = \begin{pmatrix} S & jD & 0 \\ -jD & S & 0 \\ 0 & 0 & P \end{pmatrix} \tag{2.2}$$

the Stix parameters [10] are defined:

$$S = 1 - \sum_\xi \frac{\omega_{p\xi}^2(\omega - j\nu_\xi)}{\omega[(\omega - j\nu_\xi)^2 - \omega_{c\xi}^2]} \tag{2.3}$$

$$D = \sum_\xi \frac{\sigma_\xi \omega_{c\xi}}{\omega} \frac{\omega_{p\xi}^2}{[(\omega - j\nu_\xi)^2 - \omega_{c\xi}^2]} \tag{2.4}$$

$$P = 1 - \sum_\xi \frac{\omega_{p\xi}^2}{\omega(\omega - j\nu_\xi)} \tag{2.5}$$

where $\omega_{p\xi} = \sqrt{(n_\xi q_\xi^2)/(\epsilon_0 m_\xi)}$ is the plasma frequency, σ_ξ indicates the particle charge sign, $\omega_{c\xi} = \sigma_\xi q_\xi B_0/m_\xi$ is the gyrofrequency, and ν_ξ is the collision frequency. The subscript

ξ refers to the index of the plasma species. In particular $\epsilon_{\mathbf{r}}$ is assumed to be function of position, so profiles of plasma density, etc. can be taken into account.

We assume all the metallic parts as PEC, and we model the antenna excitation by means of the voltage gap generator, which requires setting the voltage V_G at the circuit port and computing the current I_A therein [31], [32], [33]. The EM response is described with an unknown electric surface density $\mathbf{J_A}$. The currents $\mathbf{J_A}$ and $\mathbf{J_P}$ constitute the two unknowns of the problem.

2.2 Governing Equations

Two integral equations, a Volume Integral Equation (VIE) and a Surface Integral Equation (SIE), are written to solve the two unknowns $\mathbf{J_A}$ and $\mathbf{J_P}$.
We apply the boundary conditions on the antenna surface SA, which states that the tangent component of the electric field upon a PEC surface, $\mathbf{E_A}|_{tan}$, is zero. Splitting $\mathbf{E_A}$ into three parts contributed by different sources, we can write

$$[\mathbf{E^s_{AA}}(\mathbf{r}) + \mathbf{E^s_{AP}}(\mathbf{r}) + \mathbf{E^i_{AA}}(\mathbf{r})]|_{tan} = \mathbf{0} \qquad \mathbf{r} \in S_A \tag{2.6}$$

where $\mathbf{E^s_{AA}}$ and $\mathbf{E^s_{AA}}$ are the electric field radiated respectively by $\mathbf{J_A}$ and $\mathbf{J_P}$ onto S_A, $\mathbf{E^i_{AA}}$ is the impressed field in the voltage gap approximation.
We express the total electric field in the plasma region as

$$\mathbf{E_P}(\mathbf{r}) = \mathbf{E^s_{PA}}(\mathbf{r}) + \mathbf{E^s_{PP}}(\mathbf{r}) \qquad \mathbf{r} \in V_P \tag{2.7}$$

where $\mathbf{E^s_{PA}}(\mathbf{r})$ and $\mathbf{E^s_{PP}}(\mathbf{r})$ represents the secondary electric field produced by $\mathbf{J_A}$ and $\mathbf{J_P}$ within V_P.
By enforcing the boundary condition for S_A, and Eq. 2.7 we arrive at the following set of coupled surface and volume integral equations:

$$-j\omega\mu_0\bar{\mathbf{G}}(\mathbf{r}) \overset{*}{\cdot} \mathbf{J_A} + \omega^2\mu_0\bar{\mathbf{G}}(\mathbf{r}) \overset{*}{\cdot} [(\mathbf{I} - {\epsilon_{\mathbf{r}}}^{-1}) \cdot \mathbf{D_P}] + \mathbf{E^i_{AA}}(\mathbf{r})|_{tan} = \mathbf{0} \qquad \mathbf{r} \in S_A \tag{2.8}$$

$${\epsilon_{\mathbf{r}}}^{-1} \cdot \mathbf{D_P} = k_0^2\bar{\mathbf{G}}(\mathbf{r}) \overset{*}{\cdot} [(\mathbf{I} - {\epsilon_{\mathbf{r}}}^{-1}) \cdot \mathbf{D_P}] - j\omega\epsilon_0\mu_0\bar{\mathbf{G}}(\mathbf{r}) \overset{*}{\cdot} \mathbf{J_A} \qquad \mathbf{r} \in V_P \tag{2.9}$$

where $\bar{\mathbf{G}}(\mathbf{r})$ is the dyadic Green's function in free space, and $\overset{*}{\cdot}$ denotes 3D spatial convolution and scalar product [1]. It is worthwhile to underline that the really unknowns of the last system of integral equations are $\mathbf{J_A}$ and $\mathbf{D_P}$; from a numerical standpoint it is better to solve for $\mathbf{D_p}$ rather than $\mathbf{J_p}$.
In particular from the knowledge of $\mathbf{D_P}$, and hence of $\mathbf{J_P}$ and $\mathbf{E_P}$, we have the power transferred to the plasma:

$$Pw = \frac{1}{2}Re\int_{V_P} \mathbf{J^*_P} \cdot \mathbf{E_P} d^3r \tag{2.10}$$

On the other hand from the knowledge of $\mathbf{J_A}$ it is possible to compute the current flowing at the antenna port, I_A, and therein the power radiated by the antenna. However at frequency values typical for plasma thruster applications the power radiated by the antenna into free space is negligible. Therefore, we can regard the average power transferred by the generator to the antenna as a good estimation of Pw.

2.3 Numerical Solution

We numerically solve the system of Eqs.2.8, 2.9 by means of the MoM in the form of Galerkin. To this purpose, we model S_A with a 3D triangular-faceted mesh, and V_P with a tetrahedral mesh. We associate surface and volume div-conforming vector linear element

[1] In this work the scalar product between two complex numbers $a, b \in \mathbb{C}$ is $a \cdot b = ab$.

$\mathbf{f}(\mathbf{r})$ and $\mathbf{v}(\mathbf{r})$ respectively with the inner edges of the triangular mesh, and with all facets of the tetrahedral mesh (see Appendix A,B) in order to expand the unknowns as follow:

$$\mathbf{J_A} = \sum_{n=1}^{N_A} \mathbf{f_n}(\mathbf{r}) J_n \qquad \mathbf{r} \in S_A \tag{2.11}$$

$$\mathbf{D_P} = \sum_{n=1}^{N_P} \mathbf{v_n}(\mathbf{r}) D_n \qquad \mathbf{r} \in V_P \tag{2.12}$$

Substituting Eqs.2.11, 2.12 into Eqs. 2.8, 2.9, and projecting them respectively onto $\mathbf{f_m}$, $m = 1, \ldots, NA$, and onto $\mathbf{v_q}$, $q = 1, \ldots, NP$, we obtain the final algebraic system of rank $N_A + N_P$. In matrix form, it reads

$$\begin{pmatrix} [Z_{AA}] & [Z_{AP}] \\ [Z_{AP}] & [Z_{PP}] \end{pmatrix} \begin{pmatrix} Z_0[J_A] \\ [D_P]/\epsilon_0 \end{pmatrix} = - \begin{pmatrix} [V_G] \\ [0] \end{pmatrix} \tag{2.13}$$

where $Z_0 = \sqrt{\mu_0/\epsilon_0}$ and ϵ_0 have been factored out and paired with the vectors of unknown coefficients to improve the conditioning of the matrix. With this positions, $Z_0[J_A]$ and $[D_P]/\epsilon_0$ carry the physical dimensions of an electric field. The column vectors $[J_A]$ and $[D_P]$ contain the coefficients of $\mathbf{J_A}$ and $\mathbf{D_P}$ respectively.

2.4 ADAMANT user guide

Now we are going to give some guidelines to use ADAMANT. There are mainly three phases in running ADAMANT: preprocessing, numerical solution, and postprocessing. We describe the process to follow in each phase to run a simulation in the right way.

2.4.1 Pre-Processing

GMSH [42] is the free finite element mesh generator used to draw the geometries. We first draw the plasma volume, and we mesh it in tetrahedral elements. In Figs.2.1(a),(b) a plasma column mesh example is pictured. Fig.2.1(b) shows a plane cut of the plasma cylinder's mesh emphasizing the tetrahedral discretization of the volume. The characteristic length of the tetrahedral element can be set for each point drawn, this allow to control the mesh size. The mesh is exported as $*.msh$ file to be processed by a mesh converter that generates a $*.vie.msh$ file. The $*.vie.msh$ file is composed of four blocks:

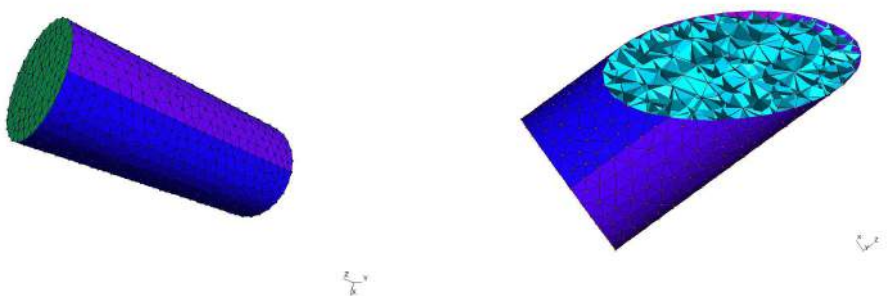

(a) (b)

Figure 2.1: (a) A plasma column mesh example, and (b) a particular of the plasma cylinder mesh, transversely cut .

1. The first block contains the information about the vertexes of the mesh tetrahedra. It is composed of five columns. The first reports the flag 1 that identifies the vertex block, the second contains the number of each vertex, and the last three contain respectively the x, y, and z coordinates of each vertex;

2. The second block contains the information about the triangles of the mesh tetrahedra. It is composed of six columns. The first reports flag 2 that identifies the triangle block, the second contains the number of each triangle. The third, fourth, and fifth columns contain the numbers corresponding to the three vertexes composing the triangle, and the sixth reports the area of each triangle;

3. The third block contains the tetrahedron information. It is composed of twenty-two columns. The first reports the flag 3 that identifies the tetrahedron block, the second contains the number of each tetrahedron, the next four columns report the identifying number of the four triangles that compose the tetrahedron, the next three columns report the barycenter coordinates, the tenth reports the tetrahedron volume. The last twelve columns contain the (x; y; z) components of the normals to each facet of the tetrahedron;

4. The fourth block contains the SWG information. It is composed of four columns. The first reports the flag 4 that identifies the SWG block, the second contains the number of each function (this correspond to the number of the triangle where the considered SWG is defined). The last two columns contains the identifying number of the two adjoining tetrahedrons on which the SWG is defined.

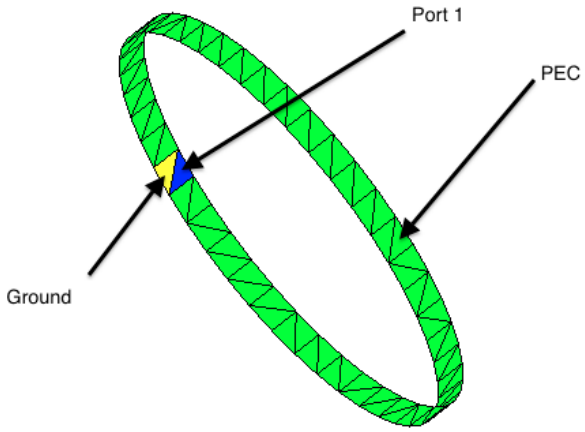

Figure 2.2: Single loop antenna mesh example

The antenna surface has PEC material properties assigned. The antenna geometry is meshed in triangular elements, as shown in Fig.2.2. The feeding is applied by setting the port region composed by at least one couple of adjoining triangles, this is consistent with the voltage gap approximation. One of the two triangles of the port region has ground material properties, the other port properties. It is possible to set up a maximum of four independent voltages, each in a different port region. The antenna mesh file must be exported as $*.inp$

file and be processed by the appropriate mesh converter. The mesh converter generates a $*.ant.msh$ file, that is composed of three blocks:

1. The first contains the information about the vertexes of the mesh triangles, it is composed of five columns. The first reports the flag 1 that identifies the vertex block, the second contains the number of each vertex, and the last three columns contain respectively the x, y, and z coordinates of each vertex;

2. The second block contains the triangle information. It is composed of six columns. The first reports the flag 2 that identifies the triangle block, the second contains the number of each triangle, in the next three columns there is the number of the vertex composing each triangle, and the last column has a flag that identify the material properties assigned to that triangle. The latter can be 0, 1, 11, 12, 13 or 14, indicating respectively the PEC, ground, port 1, port 2, port 3 or port 4 material properties.

3. The third block contains the RWG information, it is composed of five columns. The first reports the flag 3 that identifies the RWG block, the second contains the number of each function, the next two columns report the identifying numbers of the two adjoining triangles on which the RWG is defined.

2.4.2 Solution

ADAMANT needs four input files to run:

1. the $*.vie.msh$;

2. the $*.ant.msh$;

3. the *plasma.inp*;

4. the *adamant_data.inp*.

In the *adamant_data.inp* file there are the simulation parameters. This file is composed of ten blocks:

geometry contains the mesh converted file names, respectively for the surface and the volume ;

settings it contains parameters related to the settings of the simulation:

1. the source type, it can be plain wave or voltage gap. If the source type is set as voltage gap, the code needs that in the mesh converted some adjoining triangles have respectively ground and port material properties;
2. the dielectric type, it can be dielectric or plasma. The code needs respectively a dielectric.inp or plasma.inp file to run.
3. the number of samplings, where the electric fields are evaluated in the far field region;
4. the number of samplings, where the electric fields are evaluated in the far field region;

plasma it contains:

1. a flag that is the element symbol of the gas ionized, and can be:
   - Ar,
   - N2,
   - H2,
   - He,

- Ne;

2. the number of charged species;
3. the magneto-static field intensity [T];
4. the neutral background pressure [mTorr];

param reports the number of ports in the antenna geometry;

impedance is the reference impedance for each port [Ω]; it contains four complex numbers, one for each port;

voltages is the voltage gap feeding each port [V];

frequency is divided into two rows. The first reports the simulation working frequency [Hz], while the second is a threshold parameter for the code;

Sintegration defines the surface numerical integration formulas;

Vintegration defines the volume numerical integration formulas;

background reports the relative electric permittivity, and the relative magnetic permeability of the background medium.

Here follows an example:

```
&geometry
Sgeoname = ''ANTENNA MESH NAME''
Vgeoname = ''VOLUME MESH NAME''
/
&settings
sourcetype = ''voltagegap''
dieltype = ''plasma''
ntheta = 180
nphi = 180
debugging = 0
/
&plasma
gas = ''Ar''
species = 2
Bzconf = 0
Npress = 1.5d1
/
&param
nports = 1
/
&impedance
Zref(1) = 50.0d0
Zref(2) = 50.0d0
Zref(3) = 50.0d0
Zref(4) = 50.0d0
/
&feeding
voltages(1) = (1.0d0,0.0d0)
voltages(2) = (1.0d0,0.0d0)
voltages(3) = (1.0d0,0.0d0)
voltages(4) = (1.0d0,0.0d0)
/
```

```
&frequency
fsim = 125d6
dcellmax = 0.25
/
&Sintegration
dthreshold = 3.0d0
ord1(1:2) = 4 4
ord2(1:2) = 4 4
ord3(1:2) = 4 4
ord4(1:2) = 4 4
/
&Vintegration
sord1(1:2) = 1 3
sord2(1:2) = 1 3
sord3(1:2) = 3 4
sord4(1:2) = 3 4
vord1(1:2) = 1 3
vord2(1:2) = 1 3
vord3(1:2) = 3 4
vord4(1:2) = 3 4
/
&background
epr = (1.0d0,0.0d0)
mur = (1.0d0,0.0d0)
/
```

The plasma.inp file contains the plasma parameters related to each charged specie that compose the plasma. This file is structured in two blocks, one for each species. Each block is composed by six rows:

1. the name of the species considered in the block;
2. the charge [C];
3. the mass [Kg];
4. the density [m^{-3}];
5. the temperature [eV];
6. a flag representing the plasma collisionality, that can be either 1 if the plasma is collisional, or 0 if it is not.

Here follows an example:

```
#species
"electrons"
-1.602176462d-19
9.10938188d-31
1.0d+19
3.000000d+00
1
#
#species
"ions"
+1.602176462d-19
```

```
6.63367652e-26
1.0d+19
3.0000000d-02
1
#
```

2.4.3 Running ADAMANT

ADAMANT can be run by typing
> `./adamant`
on the command line.

2.4.4 Post-Processing

ADAMANT generates seven outputs files:

adamant DIELECTRIC D.txt reports the total dielectric flux density distribution in the plasma volume. It is composed of four columns. In the first column there is the port number associated with the solution of the EM problem, in the second the SWG function number, and the last two indicate respectively the real, and imaginary part of the electric flux density coefficient (D_p) for the p-th SWG function.

Pabs.txt contains the total power deposited in the plasma volume.

Prad.txt contains the total power irradiated in the far field region.

adamant PEC param.txt contains the real and imaginary parts of the admittance, impedance, S parameters for each port combination, and the input power in different blocks. Each block is composed by four columns, the first two reporting the ports associated with the solution, and the last two respectively the real and imaginary parts of the parameter considered. In the input power block, the first two columns report the value 0.

adamant PEC Ja.txt contains the information related to the current distributed onto the metal surface. It is composed of four columns. The first reports the port number associated with the solution of the EM problem, the second is the RWG number, and the last two indicate respectively the real, and imaginary part of the current coefficient (I_n) for the n-th RWG function.

Es farzone Dp.txt contains the electric far field intensity due to the contribution of $\mathbf{D_P}$, evaluated in the far field region.

Es farzone JaDp.txt contains the electric far field intensity due to the contribution of both $\mathbf{J_A}$ and $\mathbf{D_P}$, evaluated in the far field region.

Chapter 3

Mesh Analysis

We are going to model the coupling of the wave propagation and the plasma transport, in a Helicon plasma source, studying separately the electromagnetic and the plasma dynamics phenomena. The reciprocal interactions are modeled through an iterative loop. In this work, the ADAMANT code will solve for the electromagnetic coupling between the antenna and the plasma discharge. Two fluid solvers will be used, namely: (i) a zero-dimensional model called Global-Model that solves for the uniform values of the plasma parameters (e.g. plasma density) within the discharge; (ii) a one-dimensional model that solves for the radial profiles of the plasma parameters. The methodology followed to mesh the RF antenna and the plasma volume is the same with both the fluid solver coupled with ADAMANT. However in coupling ADAMANT with the one-dimensional fluid solver a particular attention must be paid to avoid the introduction of numerical noise.

If ADAMANT is coupled with a zero-dimensional fluid solver, whose input is the total power deposited in the plasma discharge, it is required a mesh that allows the calculation of this power with a good accuracy and in a reasonable time. Otherwise if ADAMANT is coupled with a one-dimensional fluid solver, whose input is a radial power profile, the local power deposition is to be sampled on a structured radial mesh. Both the plasma mesh and the number of radial nodes where the power is evaluated must be chosen in order to avoid the introduction of numerical noise as well as to give accurate results in a reasonable time.

3.1 ADAMANT and the Zero-Dimensional Fluid Solver

The accuracy of the numerical results and the computational cost of the simulation depend on the number of basis functions RWGs/SWGs (see appendix A,B). Those numbers are respectively related to the number of triangular elements in which the antenna (modeled as a 2D surface [25]) is discretized, and to the number of tetrahedral elements in which the plasma volume is discretized. Thence we can relate our results to the number of RWGs and SWGs instead of to the number of triangular and tetrahedral elements.

A rule of thumbs used to create the mesh is:

- the mesh must provide a good representation of both the antenna and the plasma geometry;
- we need to have at least 10 triangular (tetrahedral) mesh element for the maximum wave length λ_0;
- the areas of the antenna mesh triangles, and that of the tetrahedron facets in the plasma volume should be as similar as possible.

Since in our case λ_0 is in the order of the meter and our antenna geometries are one order smaller, the dimension of triangular elements used to have a good geometrical representation of the antenna geometry fully satisfy the first and the second sentences of the rule of thumbs.

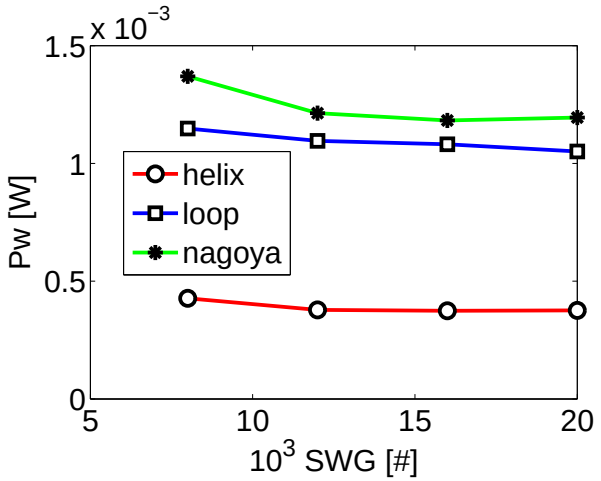

Figure 3.1: Trend of the absorbed power by the plasma discharge varying the number of SWGs. Analyzed Fractional Helix, Single-Loop, and Nagoya Type-III antennas. Plasma parameters: $n = 10^{19}$ m^{-3}, T_e=3 eV, B_0=100 G, p_n=20 mTorr, f=13.56 MHz, ΔV=1 V.

Unluckily the three guidelines presented so on are not sufficient to mesh the plasma volume in a suitable way. We need to sample adequately the polarization current in order to calculate accurately the deposited power in the plasma discharge, therefore the number of SWGs must be higher than that required from the rule of thumbs. We have considered different numbers of SWG functions varying from 8000 to 20000; in fact increasing to much the number of mesh elements we can have numerical instabilities. The accuracy of the numerical result, for different numbers of SWGs, is evaluated through the deposited power onto the plasma discharge since this is the input of the zero-dimensional fluid solver. In Fig.3.1 we have analyzed how the number of SWGs affects the power deposited onto the plasma discharge. This test has been done for three different antennas, namely a Single-Loop, a Fractional Helix, and a Nagoya Type-III antenna. It is possible to see an asymptotic behavior when the number of SWG increases. We have chosen a plasma column with approximately 12000 SWGs because this is considered the best trade-off between the accuracy of the simulation and the computing time.

Once we have identified the range of SWGs, we have done another analysis in order to find the plasma mesh where the tetrahedra are as much regular as possible and have approximately the same size one each other. Indeed the regularity of the mesh is related to the numerical stability of the system. In Fig.3.2 it is evaluated the deviation of our actual mesh from the ideal case, where all the tetrahedra are regular and equal, by means of four mesh parameters. It is reported: (i)the ratio between the radius of the circumscribed and the inscribed sphere of each tetrahedron (see Fig.3.2(a)), this ratio for a regular tetrahedron is 3; (ii) the position of the barycenters of the tetrahedra along the axial direction, in the ideal case the barycenters are distributed homogeneously (see Fig.3.2(b)); (iii) the length of the medium side of each tetrahedron (see Fig.3.2(c)), in an ideal mesh each tetrahedron has the same dimension; (iv) the volume of each tetrahedron (see Fig.3.2(d)). In conclusion for the plasma column we have chosen 12206 SWG functions as a compromise between accuracy and computing time.

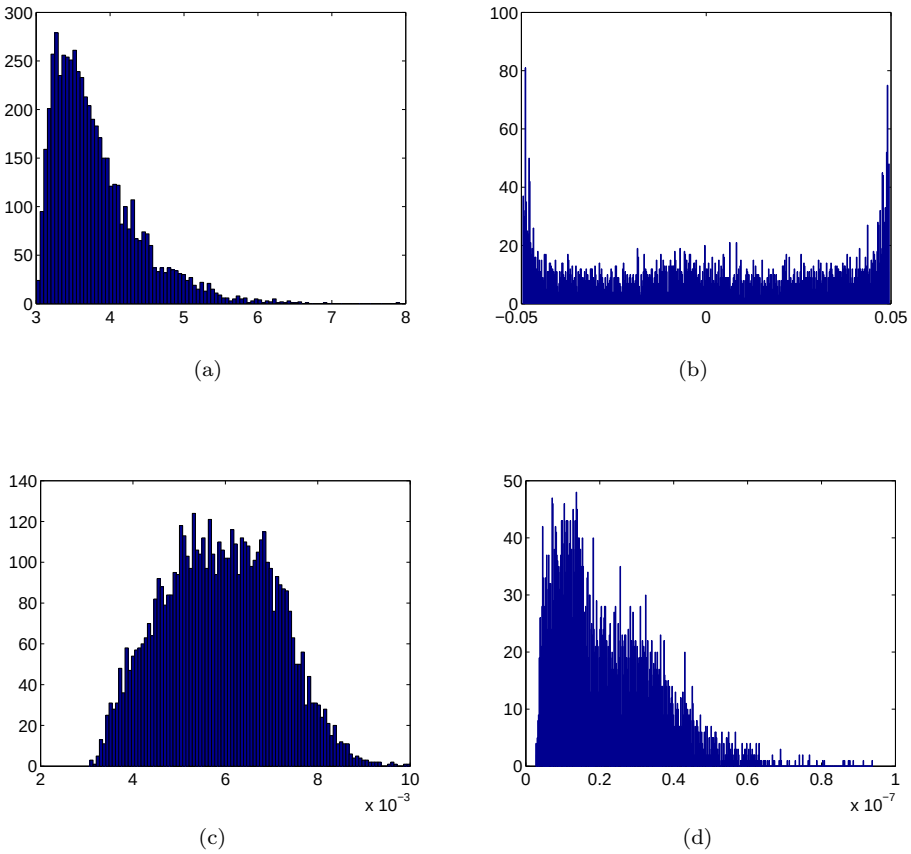

Figure 3.2: Distribution of mesh parameters: (a) the ratio between the radius of the circumscribed and the inscribed sphere of each tetrahedron; (b) the position of the barycenters of the tetrahedra along the axial direction; (c) length of the medium side of each tetrahedron; (d) volume of each tetrahedron.

3.2 ADAMANT and One-Dimensional Fluid Solver

In the following section we will give a description of the procedure to calculate a radial power deposition profile from the ADAMANT output files, and then we will focus on the mesh analysis.

3.2.1 Radial Power Profile Calculation

We have calculated the radial power profile dividing the plasma volume in a constructed radial mesh composed of N cylindrical coaxial shells. In fig.3.3 we have both the outer radius of the j-th shell (called j) and the inner radius (called $j-1$) identified by a black circle, and the j-th radial node (called $j-1/2$) identified by a white diamond. The radial nodes are the points in which the radial power profile is sampled. It is worthwhile to underline that: (i)the distance between j and $j-1$ is fixed and equal to $\Delta r = R/N$, where R is the plasma cylinder radius; (ii) the distance between j and $j-1/2$ (respectively $j-1$ and $j-1/2$) is fixed and equal to $\Delta r/2$.

Customized MATLAB scripts have been developed in order to calculate the radial power profile starting from the ADAMANT input and output files. Specifically only the $*.vie.msh$ input file and the *adamant DIELECTRIC_D.txt* output file (see Chapter 2) are necessary for our purpose. From the *adamant DIELECTRIC_ D.txt* file we have the value of each SWG,

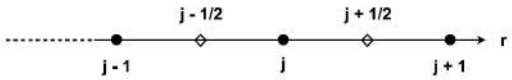

Figure 3.3: Graphical sketch of the radial constructed mesh used in the calculation of the power deposition profile: (i) the black circles are the delimiters of the coaxial cylindrical shells, j and $j-1$ delimit the j-th shell; (ii) the white diamonds are the radial nodes where the deposited power is sampled, $j-1/2$ is related to the j-th shell.

from the 4th block of the $*.vie.msh$ file we have the SWGs that contribute in the calculation of the electric flux density inside of each tetrahedron. Combining this information with the definition of SWG (see Appendix B) it is possible to calculate the electric flux density $\mathbf{D_P}_i$ in the barycenter of the i-th tetrahedron and then, from Eq.(2.1), the electric current density $\mathbf{J_P}_i$. If we suppose that those two parameters are constant in each tetrahedron we have, from Eq.(2.10), that the deposited power in the considered tetrahedron is equal to $\frac{1}{2}Re(\mathbf{J_P}_i \cdot \mathbf{E_P}_i)V_i$; where V_i is the i-th tetrahedron volume. In order to calculate the radial power profile, we need to attribute the power deposited into each tetrahedron to the radial shell in which the barycenter of the considered tetrahedron lies. The set of the tetrahedra whose barycenters are in the $j-th$ shell is indicated with S_j. Therefore the radial power calculated in the j-th node of the constructed radial mesh is:

$$Pw_{r\ j} = \frac{L}{\bar{V}_j} \sum_{i \in S_j} \frac{1}{2} Re(\mathbf{J}^*_{\mathbf{P}i} \cdot \mathbf{E_P}_i) V_i \tag{3.1}$$

Where L is the plasma column length, and $\bar{V}_j = \sum_{i \in S_j} V_i$.

The validation of this model has been done through the comparison between the total power calculated as the integral of the radial power profile and as ADAMANT output (in the *Pabs.txt* file). The difference between those two values are lower than 0.01%.

3.2.2 Radial Power Profile Mesh Analysis

In the coupling of ADAMANT with a one-dimensional fluid solver the criteria described so on are not enough to guarantee an accurate solution for the power deposition profile. In

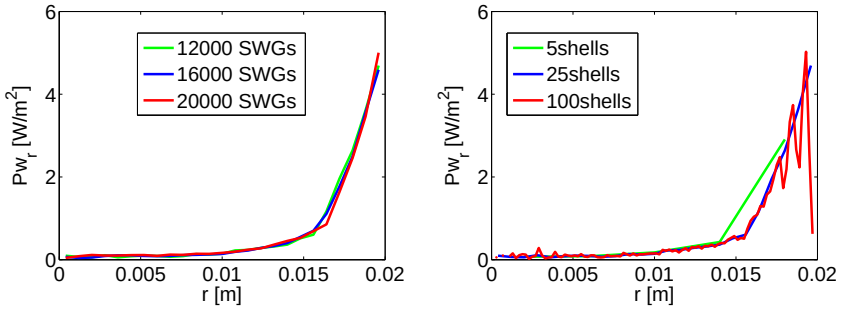

(a) (b)

Figure 3.4: Radial power deposition profile: (a)25 radial shells varying the number of SWGs; (b) approximately 12206 SWGs varying the number of radial shells. Plasma parameters: $n = 10^{19}$ m^{-3}, T_e=3 eV, B_0=100 G, p_n=20 mTorr, f=13.56 MHz, ΔV=1 V.

fact ADAMANT relies on an unstructured mesh, and calculates the power deposited into each tetrahedron. In order to calculate the radial power profile, the local power deposited is to be sampled on a structured radial mesh; specifically, the number of radial nodes is to be chosen in such a way to avoid numerical noise. In Fig.3.4 the radial power profile is evaluated for different combination of the number of SWGs and the number of radial nodes. The number of mesh elements does not influence the radial profile in a relevant way (see Fig.3.4(a)), reversely the number of radial shells is a critical parameter for the calculation of the radial power profile (see Fig.3.4(b)). If the shells number is too high the power profile is affected by numerical noise, reversely if the shells number is too low the radial power profile is inaccurate. A rule of thumbs to evaluate the maximum number of radial nodes that does not produce numerical noise is: the distance between two consecutive radial nodes should have the same order of magnitude of the mean side of the tetrahedra. We have chosen a plasma column with 12206 SWGs and 25 radial nodes, this is considered the best trade-off between the accuracy of the simulation and the computing time.

The power deposition profile calculated with 12206 SWGs and 25 radial nodes is validated against SPIREs[24] (see Fig.3.5). This solver has been chosen since it was specifically conceived to evaluate the radial power deposition profile in magnetized plasma waveguides.

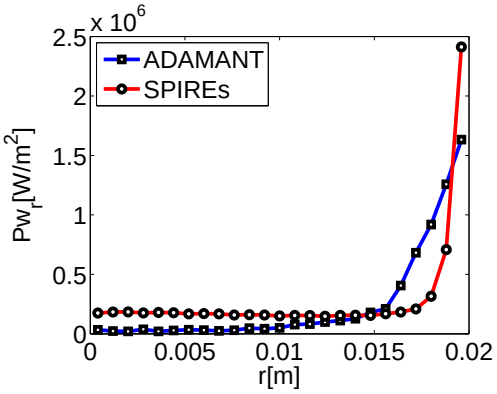

Figure 3.5: Comparison between the radial power profile evaluated by SPIREs and ADAMANT, when P_{abs}=500 W. Plasma parameters: $n = 10^{19}$ m^{-3}, T_e=3 eV, B_0=100 G, p_n=20 mTorr, f=13.56 MHz.

Chapter 4

Coupling ADAMANT and GlobalModel

To model the coupling of the wave propagation and the plasma transport it is possible to study separately the electromagnetic and plasma dynamics phenomena. These phenomena will be solved by means of an electromagnetic and a fluid solver, respectively; both solvers will be coupled by means of an iterative loop (see Fig.4.1). The loop is initialized with a first guess deposited power; the fluid solver, that solves for the plasma transport, runs first and its output quantities (e.g., plasma density) are the input for the electromagnetic solver. Similarly, the output of the electromagnetic solver (the power deposited into the plasma) is the input of the fluid solver. These two tools will iterate until convergence criteria are satisfied. From a physical point of view, this approach is justified because the time scaling at which the two phenomena happen are different, and the wave propagation is by far faster than the plasma diffusion. In the study of the plasma transport, the wave propagation can be retained as a source term through the power deposited by the antenna into the plasma; in the solution of wave propagation the plasma parameters can be considered as stationary. In

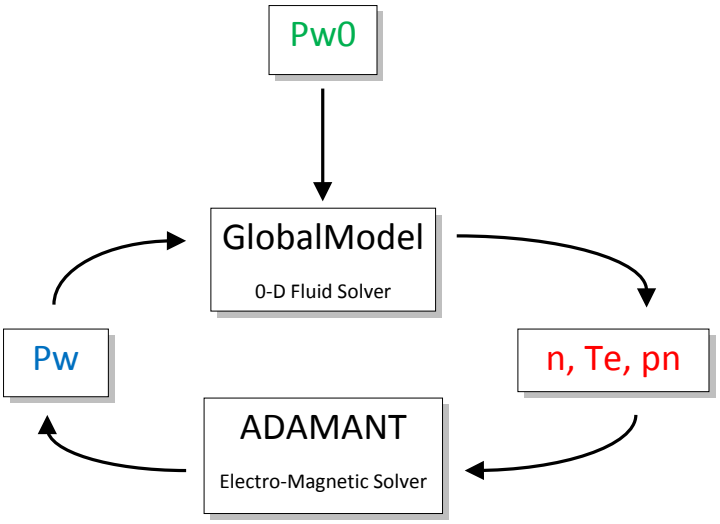

Figure 4.1: Sketch of the iterative loop: $Pw0$ is the first guess deposited power, Pw is the deposited power, n is the plasma density, T_e is the electron temperature, p_n is the neutral pressure

this chapter we present the results obtained coupling the ADAMANT code, that solves for the electromagnetic coupling between the antenna and the plasma discharge, with Global-Model[32], a zero-dimensional fluid model that solves for the uniform values of the plasma density, electron temperature, and neutral pressure within the discharge.

The reached plasma density (n), electron temperature (T_e), neutral pressure(p_n), and power absorbed by the plasma discharge (Pw) are the parameters considered to evaluate the equilibrium conditions of the source. In our model we do not consider outflows. We have investigated three different antennas, namely: (i) the Single Loop (see Fig.4.2(a)); (ii) the Nagoya type III (see Fig.4.2(b)); (iii) the Fractional Helix (see Fig.4.2(c)). These antennas are all coupled to a plasma cylinder with identical geometry, as shown in Fig.4.2, where b = 0.02 m, a = 0.03 m, w = 0.006 m, L = 0.1 m, LA = 0.05 m, t = 0.002 m and s = 0.01 m. In the simulations we have used 12206 SWGs for the plasma column, and 72 RWGs for the Single Loop, 770 for the Nagoya type-III and 748 for the Fractional Helix. The parameters considered in this study are: the magneto-static field (B_0); the initial neutral background pressure(p_{n0}); the voltage gap that drives the antenna(ΔV). All the antennas work at a frequency of 13.56 MHz. Table 4.1 summarizes the range of parameters considered, these values are typical for plasma Helicon sources.

Variable	Value
B_0 [G]	250,500,750,1000
p_{n0} [mTorr]	1,15,30
ΔV [V]	100,250,500

Table 4.1: Simulation Parameters

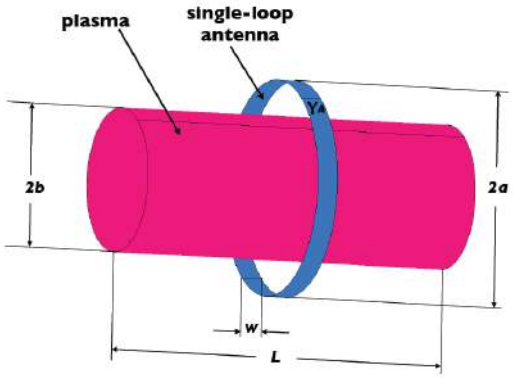

(a)

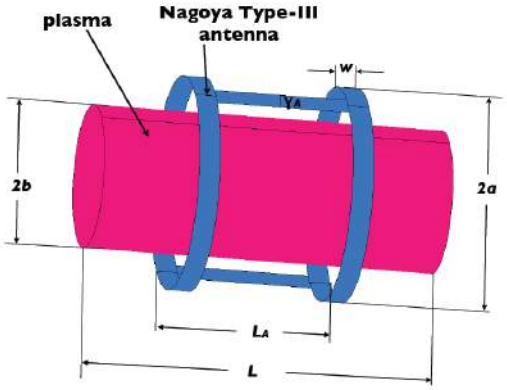

(b)

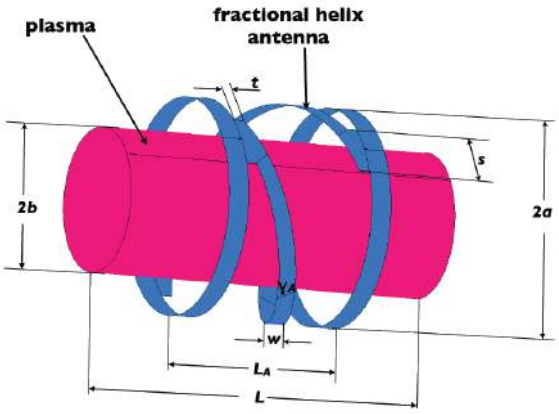

(c)

Figure 4.2: Helicon plasma source with (a) Single-Loop, (b) Nagoya type-III (c) and Fractional Helix

4.1 Iterative Loop

In this section we want to give a quick description of the iterative loop to couple ADAMANT and GlobalModel. The input of the iterative loop are the geometry of the source, p_{n0}, B_0, and ΔV; the output are n, p_n, T_e (evaluated by GlobalModel), and Pw (evaluated by ADAMANT). In our analysis GlobalModel runs first, it is initialized with a first guess Pw_0, and calculates n, p_n, T_e; with those values Pw is calculated by ADAMANT and the loop restart until the convergence is reached. The convergence criterion implemented is: the relative error between two consecutive steps must be lower than an imposed threshold value. The choice of Pw_0 is a critical parameter because its value must be higher than the lowest Pw that sustains the source. In order to avoid this problem a preliminary analysis was done to identify the minimum Pw values that sustains the source for the different configurations of p_{n0} and B_0. In Fig.4.3 are reported n and Pw for each step of the iterative loop when the antenna is a Single Loop, B_0=100 G, p_{n0}=20 mTorr, ΔV=400 V.

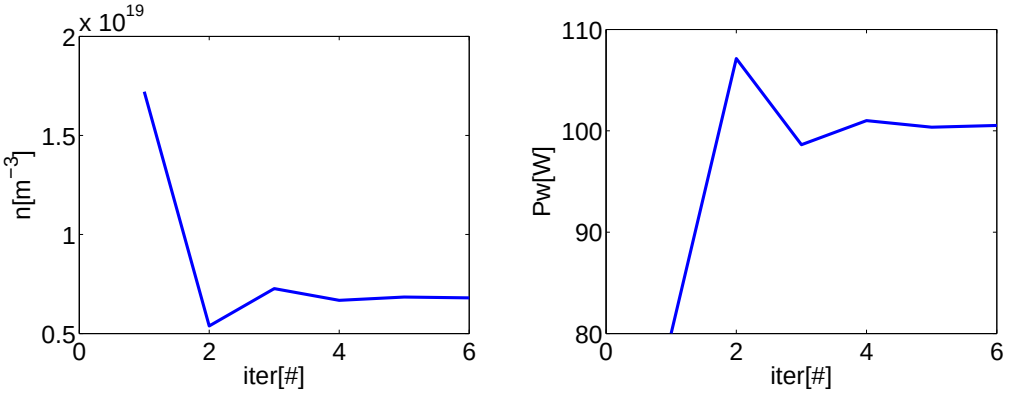

(a) (b)

Figure 4.3: Output of the iteration loop in function of the iterative step, when the antenna is a Single Loop, B_0=100 G, p_{n0}=20 mTorr, ΔV=400 V: (a) plasma density, calculated by GlobalModel, (b)absorbed power, calculated by ADAMANT.

Another way in which the iterative loop can be graphically represented is reported in Fig.4.4. If we fix the plasma discharge geometry, p_{n0}, B_0 and we run GlobalModel for different Pw we obtain n, p_n, and T_e in the steady conditions. If we plot Pw against n we have the *steady state* curve (see Fig.4.4); it is worthwhile to remember that in the x-axis we could have similarly p_n or T_e instead of n, in fact we have chosen only one parameter to describe the steady state. If we run ADAMANT, for a certain antenna and a fixed ΔV, in the steady conditions found running GlobalModel we have the power that is really absorbed by the source in those conditions; in this way we have the *absorbed power* curve (see Fig.4.4). The equilibrium point reached by the source, with the chosen antenna and ΔV, is the intersection of the two curves; in fact here the power required to sustain the source in the steady conditions is also the power absorbed. Moreover the iteration loop is represented by a sequence of points that stay on the two curves: in Fig.4.4 we have Pw_0=250 W, this means that in the steady conditions we have $n \approx 2 \times 10^{19}$ m^{-3} (point in the *steady state* curve), but in those conditions the absorbed power is $Pw \approx 100$ W (point in the *absorbed power* curve), and so on until the convergence. In particular this graphical representation can give useful information on the iterative loop: (i) if in the intersection point the absolute value of the derivate of the *absorbed power* curve is higher than the absolute value of the derivate of the *steady state* curve the iterative loop cannot be stable [43]; (ii) the *absorbed power* curve scales with ΔV^2 and the *steady state* curve is independent from ΔV, so we can have a graphical suggestion of the Pw_0 to choose in order to reach the convergence with the lowest number of iterations.

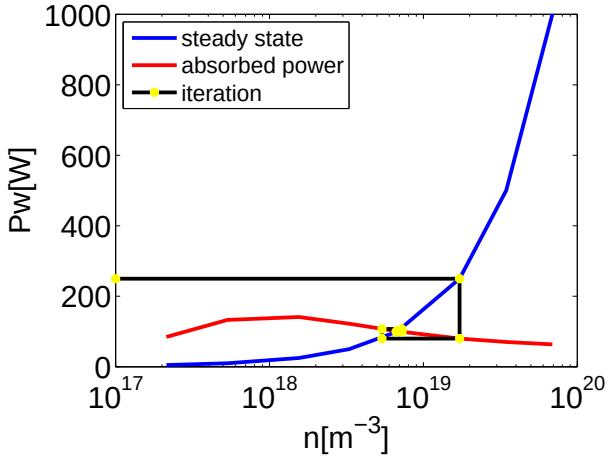

Figure 4.4: Output of the iteration loop when the antenna is a Single Loop, B_0=100 G, p_{n0}=20 mTorr, ΔV=400 V. (i) The *steady state* curve represent the stationary conditions that the source can reach; (ii) the *absorbed power* curve represent the power really absorbed by the source; (iii) the *iteration* curve represent the iterative steps: horizontal segments represent the evaluation of the steady states by GlobalModel, vertical segments represent the evaluation of the absorbed power by ADAMANT.

4.2 Single Loop Antenna

The parameters that describe the equilibrium conditions reached by the sources are reported for p_{n0} = 1 mTorr and p_{n0}=30 mTorr respectively in Fig.4.5 and Fig.4.6, those parameters are presented in function of B_0 and for three different values of ΔV. In the comparison of Fig.4.5(a) and Fig.4.5(d) (as in Fig.4.6) it is possible to notice an approximately linear dependence of the plasma density from the power deposited. Moreover increasing Pw we have a decrease of p_n (see Fig.4.5(d) and Fig.4.5(c), as in Fig.4.6) that is connected to the increase of n (in fact in our source there is not outflow), and a decrease of T_e (see Fig.4.5(d) and Fig.4.5(b), as in Fig.4.6). In particular T_e reaches the minimum value asymptotically when Pw increases, and the maximum around the minimum value of Pw that allows the source to be sustained. It is worthwhile to underline that the relations between Pw and respectively n, T_e, p_n are general; so in the following discussion we will pay more attention in the Pw trend, because all the other parameters are related to Pw in the way described right now.

Pw depends on ΔV (see Fig.4.5(d) and Fig.4.6(d)); in particular for ΔV=100 V we have that the source is not able to be sustained if B_0=250 G and B_0=500 G (see Fig.4.5(d)), reversely the same does not happen for the same values of B_0 but higher ΔV. Pw reaches the highest values if B_0 is higher than a certain threshold value (see Fig.4.5(d) and Fig.4.6(d)). In general the higher is ΔV the lower is the threshold values at which Pw reaches the maximum values (see Fig.4.5(d) and Fig.4.6(d)). In particular it is possible to notice a plateau when B_0 is higher than the so-called threshold value. If p_{n0}=30 mTorr the value of this plateau depends on ΔV, increasing ΔV also Pw grows (see Fig.4.6(d)); reversely with p_{n0}=1mTorr the plateau value is approximately independent from ΔV(see Fig.4.5(d)). This behavior is connected to the non linear dependence of the power deposited in the plasma discharge from the plasma parameters, e.g. n and T_e; in fact growing ΔV the absorbed power increases in the majority of the cases, but not always (see Fig.4.5(d) when B_0=1000 G).

In Fig.4.7 and Fig.4.8 we have the same parameters of Fig.4.5 and Fig.4.6 but for two fixed values of ΔV, ΔV=100 V and ΔV=500 V, and for three different values of p_{n0}. It is still possible to notice the opposite trend of n and T_e. In particular p_{n0} does not have

a huge influence in Pw and n (see Figs.4.8(a,d)) apart from the situations in which the source is near to the switch-off (see Figs.4.7(a,d)). Reversely we have that the minimum values of ΔV, at which the sustainment of the source is possible, is really dependent on p_{n0} and is higher for the higher values of p_{n0} (see Figs.4.7(a,d)). Also T_e is influenced by p_{n0}, in Fig.4.8(b) we can see a relevant difference between T_e with p_{n0}=1 mTorr and p_{n0} = 30 mTorr. The lower is the p_{n0} the higher is T_e also if Pw does not change (see Fig.4.7(b,d) and Fig.4.8(b,d)). The parameter that mostly depends on p_{n0} is p_n (see Fig.4.7(c) and 4.8(d)), this strong relation is due to the weakly ionization ($< 1\%$ in many cases) that is reached in those sources. Therefore for the higher values of p_{n0} the rate of ionization $r_{ion} = n/n_n$ (where n_n is the neutral density) is lower because n is not very influenced by p_{n0} and n_n has a linear dependence from p_{n0}.

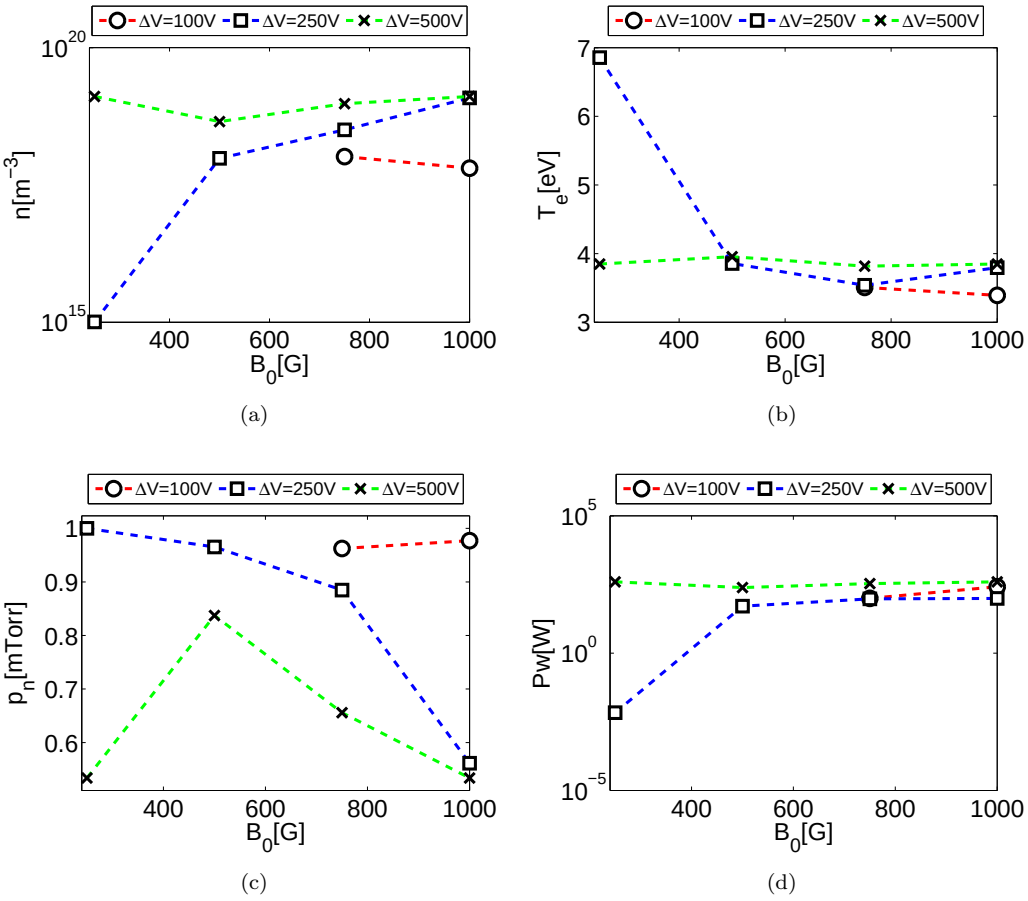

Figure 4.5: Equilibrium conditions in function of the quasi-axial magnetic field: (a) plasma density, (b) electron temperature, (c) neutral pressure, (d) absorbed power. The plasma source is driven by a Single Loop antenna, and p_{n0}=1 mTorr. We have analyzed ΔV=100 V, ΔV=250 V, ΔV=500 V.

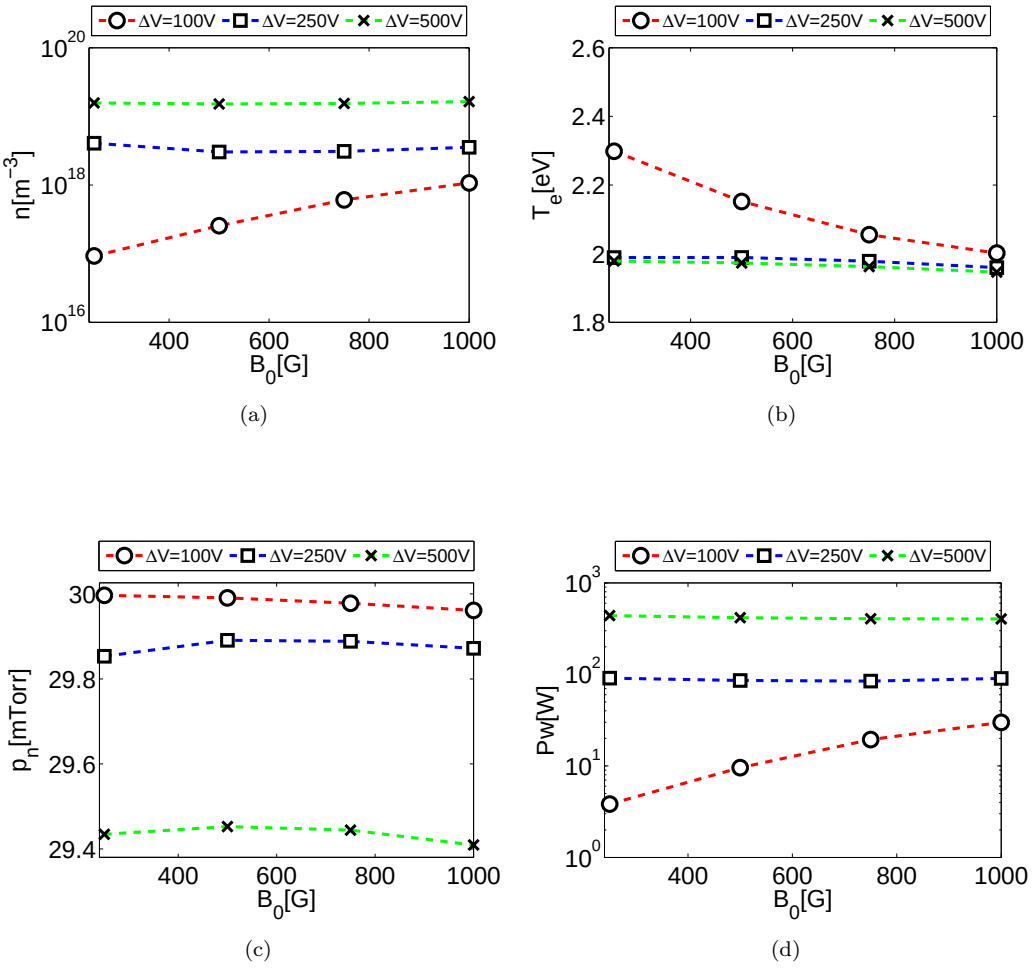

Figure 4.6: Equilibrium conditions in function of the quasi-axial magnetic field: (a) plasma density, (b) electron temperature, (c) neutral pressure, (d) absorbed power. The plasma source is driven by a Single Loop antenna, and p_{n0}=30 mTorr. We have analyzed ΔV=100 V, ΔV=250 V, ΔV=500 V.

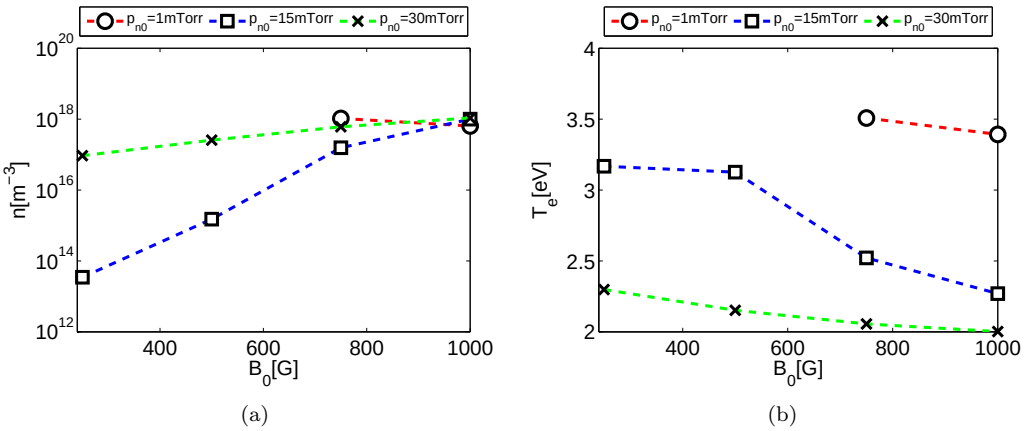

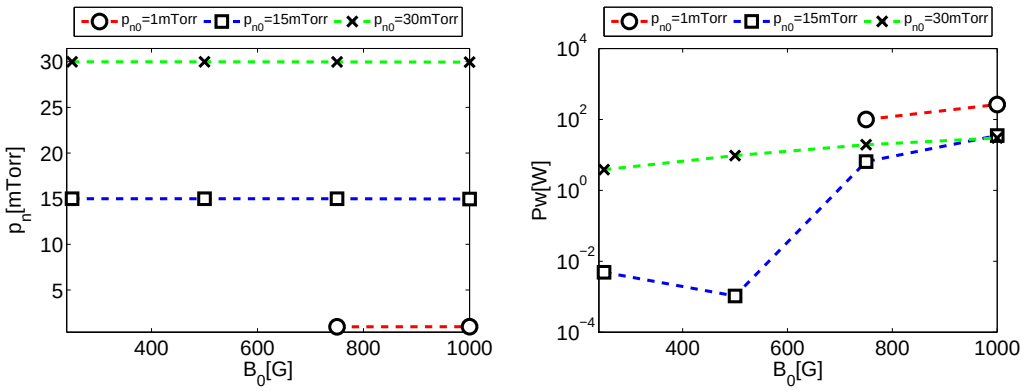

(c) (d)

Figure 4.7: Equilibrium conditions in function of the quasi-axial magnetic field B_0: (a) plasma density, (b) electron temperature, (c) neutral pressure, (d) absorbed power. The plasma source is driven by a Single Loop antenna, which is fed by ΔV=100 V. We have analyzed p_{n0}=1 mTorr, p_{n0}=15 mTorr, p_{n0}=30 mTorr.

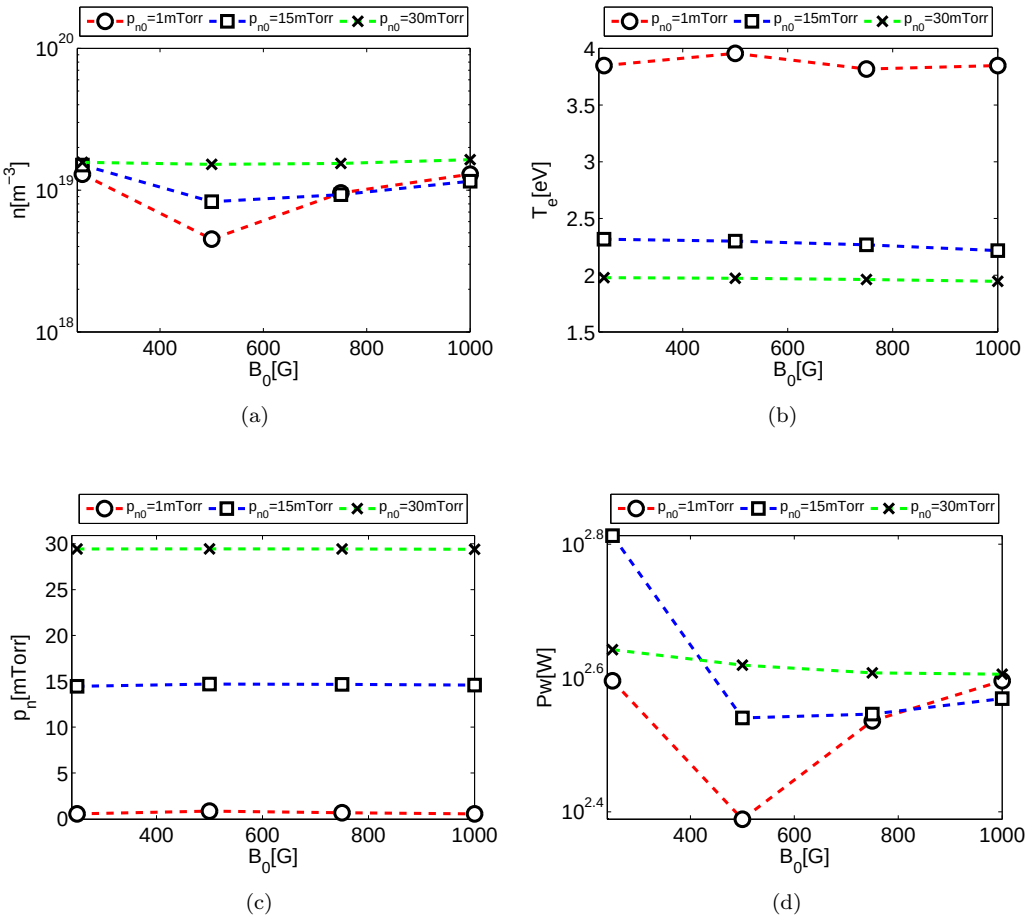

(a) (b)

(c) (d)

Figure 4.8: Equilibrium conditions in function of the quasi-axial magnetic field B_0: (a) plasma density, (b) electron temperature, (c) neutral pressure, (d) absorbed power. The plasma source is driven by a Single Loop antenna, which is fed by ΔV=500 V. We have analyzed p_{n0}=1 mTorr, p_{n0}=15 mTorr, p_{n0}=30 mTorr.

4.3 Nagoya Type-III Antenna

The parameters that describe the equilibrium conditions reached by the sources are reported for p_{n0} = 1 mTorr and p_{n0}=30 mTorr respectively in Fig.4.9 and Fig.4.10, those parameters are presented in function of B_0 and for three different values of ΔV. In the comparison of Fig.4.9(a) and Fig.4.9(d) (as in Fig.4.10) it is possible to notice the previously described linear dependence of n from Pw. Similarly increasing Pw we have a decrease of p_n (see Fig.4.9(d) and Fig.4.9(c)), and a decrease of T_e (see Fig.4.9(d) and Fig.4.9(b)).

When p_{n0}=1 mTorr, if ΔV=100 V or ΔV=250 V we have that Pw reaches the highest values for the highest values of B_0, while Pw is not really influenced by B_0 if ΔV=500 V (see Fig.4.9(d)). Reversely, if p_{n0}=30 mTorr, Pw is not really dependent from B_0 for ΔV=100 V and ΔV=500 V, while Pw decrease for the highest values of B_0 if ΔV=250 V (see Fig.4.10(d)). In both the p_{n0}=1 mTorr and p_{n0}=30 mTorr cases we have that Pw increases with ΔV. In general we have that the highest values of B_0 and ΔV allows the highest Pw, and then n, but this is not always true (see Fig.4.10(d) when ΔV=250 V).

In Fig.4.11 and Fig.4.12 we have the same parameters of Fig.4.11 and Fig.4.12 but for two fixed values of ΔV, ΔV=100 V and ΔV=500 V, and for three different values of p_{n0}. In particular p_{n0} does not have a huge influence in Pw and n (see Figs.4.11(a,d)). It is still possible to notice the opposite trend of n and T_e. However we have that T_e is particularly dependent from p_{n0} even thought n and Pw are not really dependent from p_{n0} (see Figs.4.11(b,d) and Figs4.12(b,d)). In particular for p_{n0}=1 mTorr we have a relevant growth of T_e in respect to the cases where p_{n0} is higher (see Fig.4.11(b) and Fig4.12(b)). The parameter that mostly depends on p_{n0} is p_n (see Fig.4.11(c) and 4.12(d)), this strong relation is due to the weakly ionization ($< 1\%$ in many cases) that is reached in those sources. Therefore for the higher values of p_{n0} the rate of ionization $r_{ion} = n/n_n$ (where n_n is the neutral density) is lower because n is not very influenced by p_{n0} and n_n has a linear dependence from p_{n0}.

With this antenna and in the plasma configurations analyzed we have not found any situation in which the source is not able to be sustained.

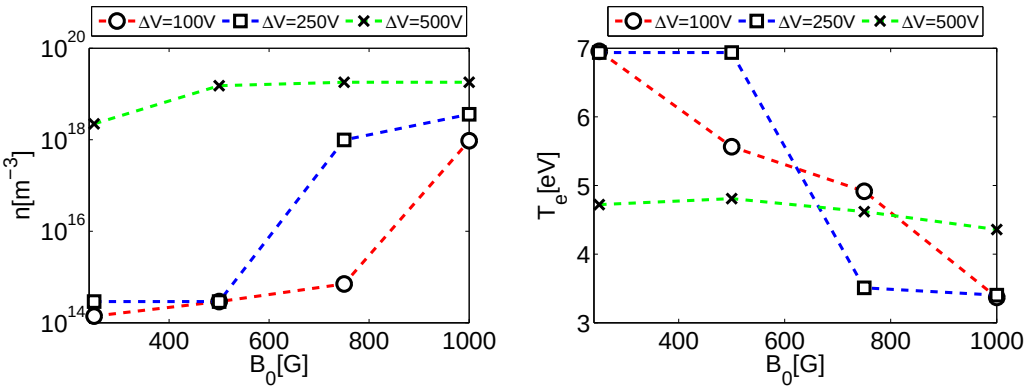

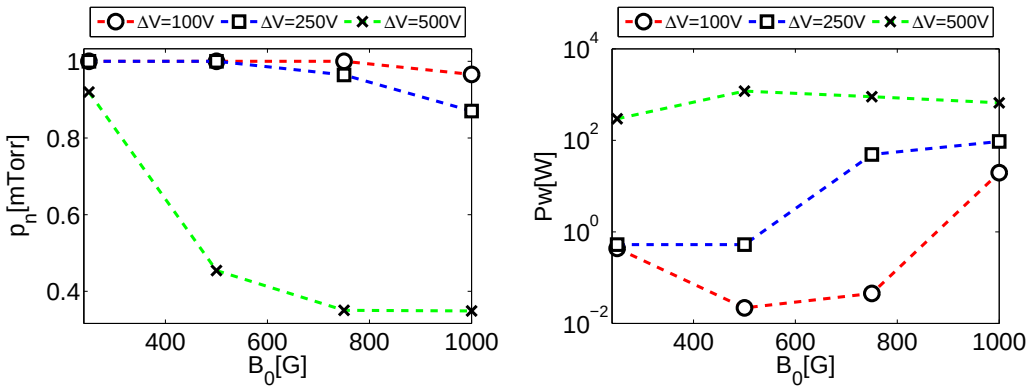

(c) (d)

Figure 4.9: Equilibrium conditions in function of the quasi-axial magnetic field: (a) plasma density, (b) electron temperature, (c) neutral pressure, (d) absorbed power. The plasma source is driven by a Nagoya Type-III antenna, and p_{n0}=1 mTorr. We have analyzed ΔV=100 V, ΔV=250 V, ΔV=500 V.

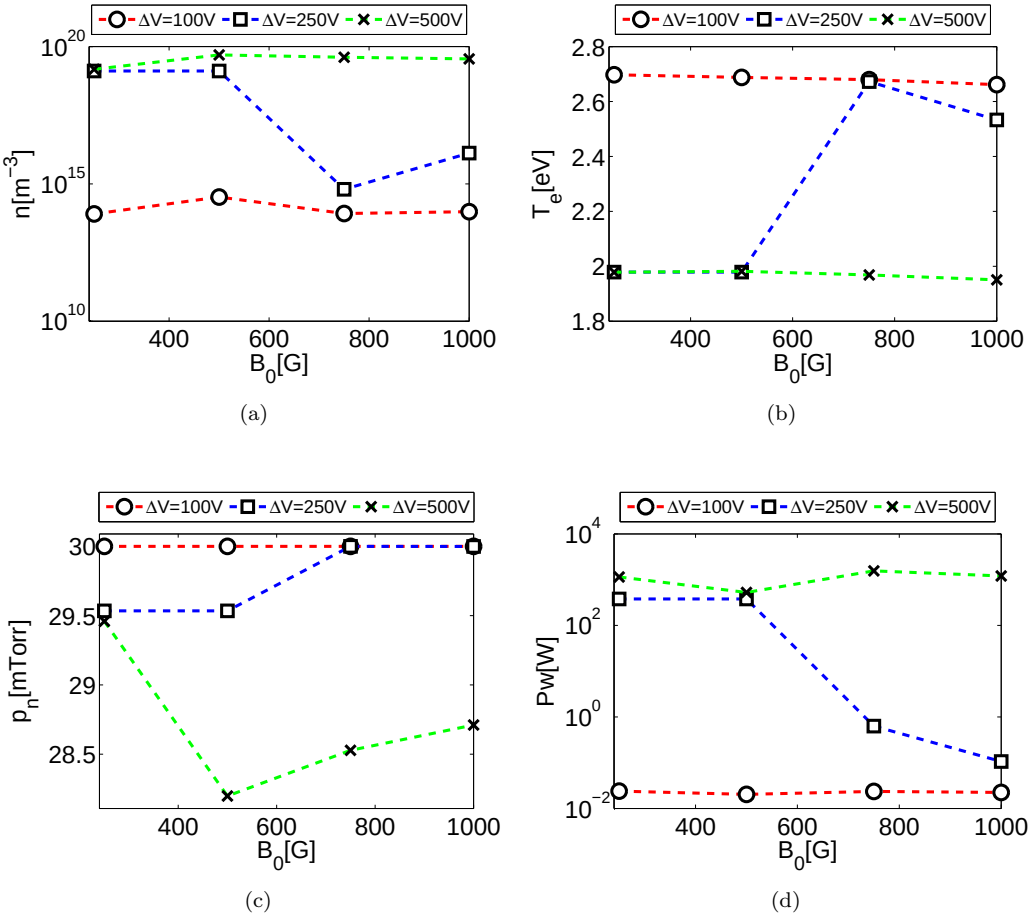

(a) (b)

(c) (d)

Figure 4.10: Equilibrium conditions in function of the quasi-axial magnetic field: (a) plasma density, (b) electron temperature, (c) neutral pressure, (d) absorbed power. The plasma source is driven by a Nagoya Type-III antenna, and p_{n0}=30 mTorr. We have analyzed ΔV=100 V, ΔV=250 V, ΔV=500 V.

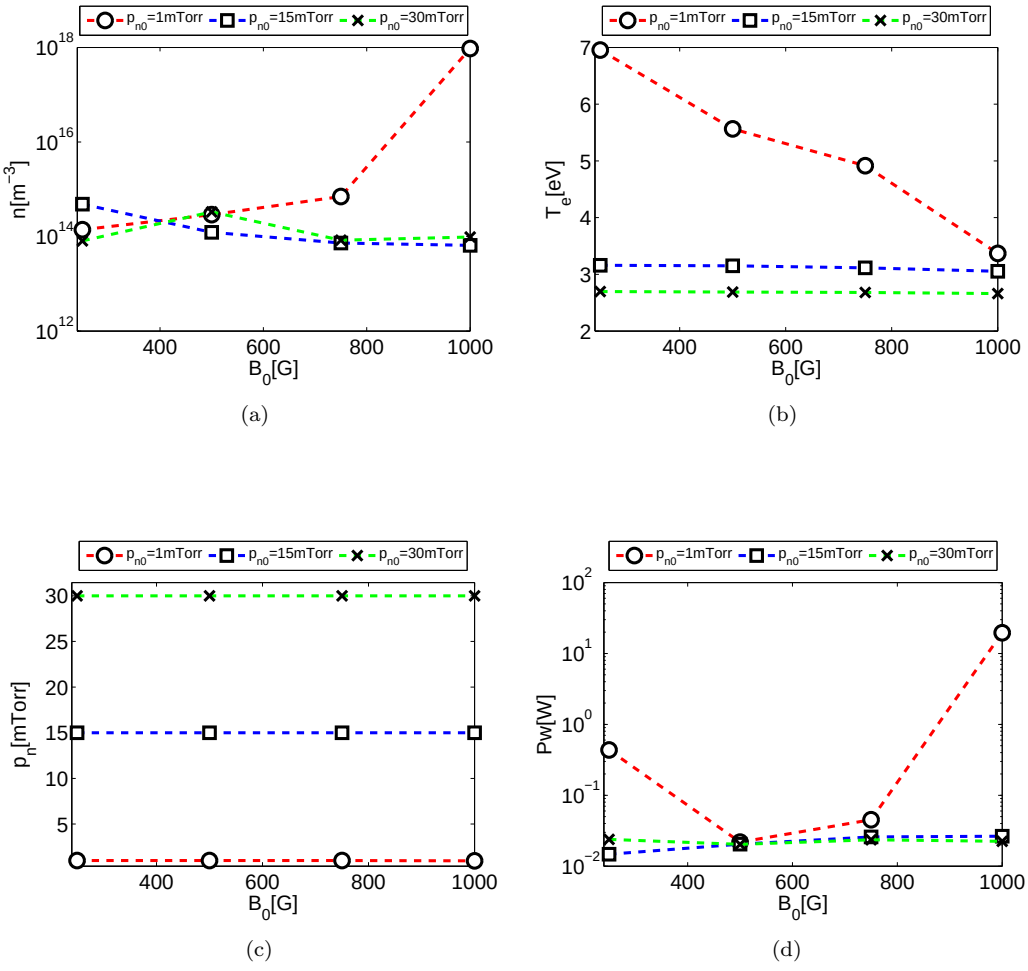

Figure 4.11: Equilibrium conditions in function of the quasi-axial magnetic field B_0: (a) plasma density, (b) electron temperature, (c) neutral pressure, (d) absorbed power. The plasma source is driven by a Nagoya Type-III antenna, which is fed by ΔV=100 V. We have analyzed p_{n0}=1 mTorr, p_{n0}=15 mTorr, p_{n0}=30 mTorr.

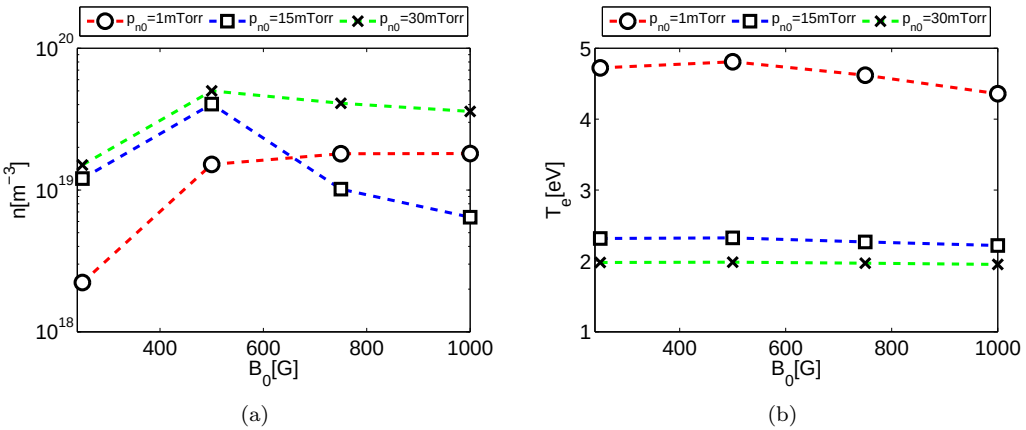

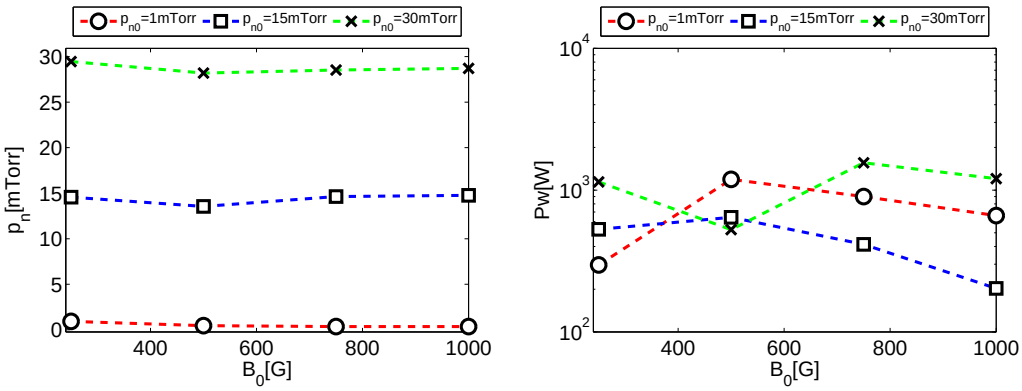

Figure 4.12: Equilibrium conditions in function of the quasi-axial magnetic field B_0: (a) plasma density, (b) electron temperature, (c) neutral pressure, (d) absorbed power. The plasma source is driven by a Nagoya Type-III antenna, which is fed by ΔV=500 V. We have analyzed p_{n0}=1 mTorr, p_{n0}=15 mTorr, p_{n0}=30 mTorr.

4.4 Fractional Helix Antenna

The parameters that describe the equilibrium conditions reached by the sources are reported for $p_{n0} = 1$ mTorr and p_{n0}=30 mTorr respectively in Fig.4.13 and Fig.4.14, those parameters are presented in function of B_0 and for three different values of ΔV. In the comparison of Fig.4.13(a) and Fig.4.13(d) (as in Fig.4.14) it is possible to notice the previously described linear dependence of n from Pw. Similarly increasing Pw we have a decrease of p_n (see Fig.4.13(d) and Fig.4.13(c), idem), and a decrease of T_e (see Fig.4.13(d) and Fig.4.13(b)).

When p_{n0}=1 mtorr, Pw reaches the highest values for the highest values of B_0, and is really dependent from ΔV(see Fig.4.13(d)); in particular Pw decrease if ΔV=100V, but there are not particular differences between the case where ΔV=250 V and ΔV=500 V(see Fig.4.13(d)). Reversely if p_{n0}=30 mtorr we have that Pw is not really dependent from B_0 (see Fig.4.14(d)); in particular for ΔV=100 V and ΔV=250 V the reached absorbed power is by far lower than for ΔV=500 V (see Fig.4.14(d)). In general we have that the highest values of B_0 and ΔV allows the highest Pw, and then n, but this is not always true (see Fig.4.13(d) for B_0=1000 G or Fig.4.14(d) for ΔV=500 V).

In Fig.4.15 and Fig.4.16 we have the same parameters of Fig.4.13 and Fig.4.14 but for two fixed values of ΔV, ΔV=100 V and ΔV=500 V, and for three different values of p_{n0}. In particular p_{n0} does not have a huge influence in Pw and n (see Figs.4.15(a,d)). It is still possible to notice the opposite trend of n and T_e. However we have that T_e is particularly dependent from p_{n0} even thought n and Pw are not really dependent from p_{n0} (see Figs.4.15(b,d) and Figs4.16(b,d)). In particular when p_{n0}=1 mtorr we have a relevant growth of T_e in respect to the cases where p_{n0} is higher (see Fig.4.15(b) and Fig.4.15(d)). The parameter that mostly depends on p_{n0} is p_n (see Fig.4.15(c) and 4.15(d)), this strong relation is due to the weakly ionization ($< 1\%$ in many cases) that is reached in those sources. Therefore for the higher values of p_{n0} the rate of ionization $r_{ion} = n/n_n$ (where n_n is the neutral density) is lower because n is not very influenced by p_{n0} and n_n has a linear dependence from p_{n0}.

With this antenna and in the plasma configurations analyzed we have not found any situation in which the source is not able to be sustained.

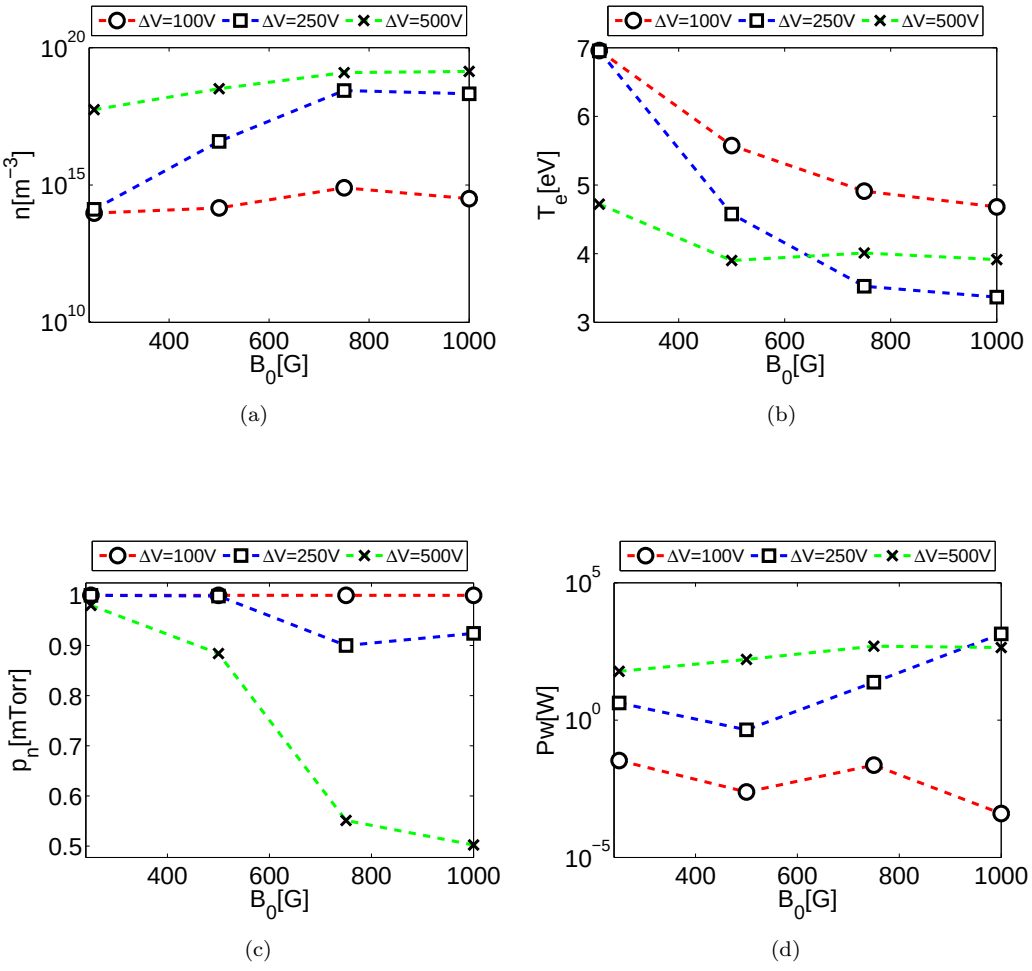

Figure 4.13: Equilibrium conditions in function of the quasi-axial magnetic field: (a) plasma density, (b) electron temperature, (c) neutral pressure, (d) absorbed power. The plasma source is driven by a Fractional Helix antenna, and p_{n0}=1 mTorr. We have analyzed ΔV=100 V, ΔV=250 V, ΔV=500 V.

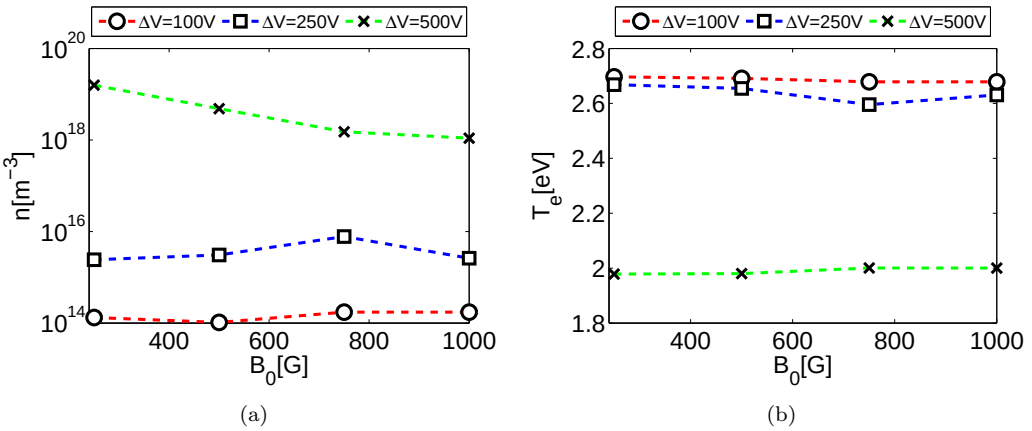

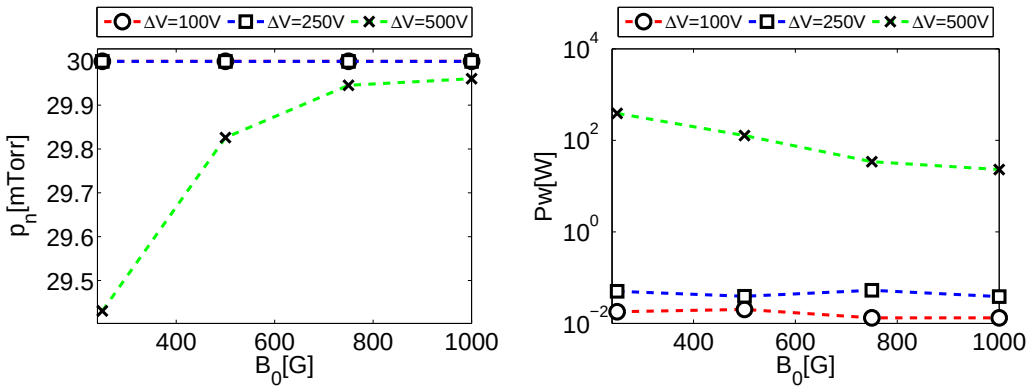

(c) (d)

Figure 4.14: Equilibrium conditions in function of the quasi-axial magnetic field: (a) plasma density, (b) electron temperature, (c) neutral pressure, (d) absorbed power. The plasma source is driven by a Fractional Helix antenna, and p_{n0}=30 mTorr. We have analyzed ΔV=100 V, ΔV=250 V, ΔV=500 V.

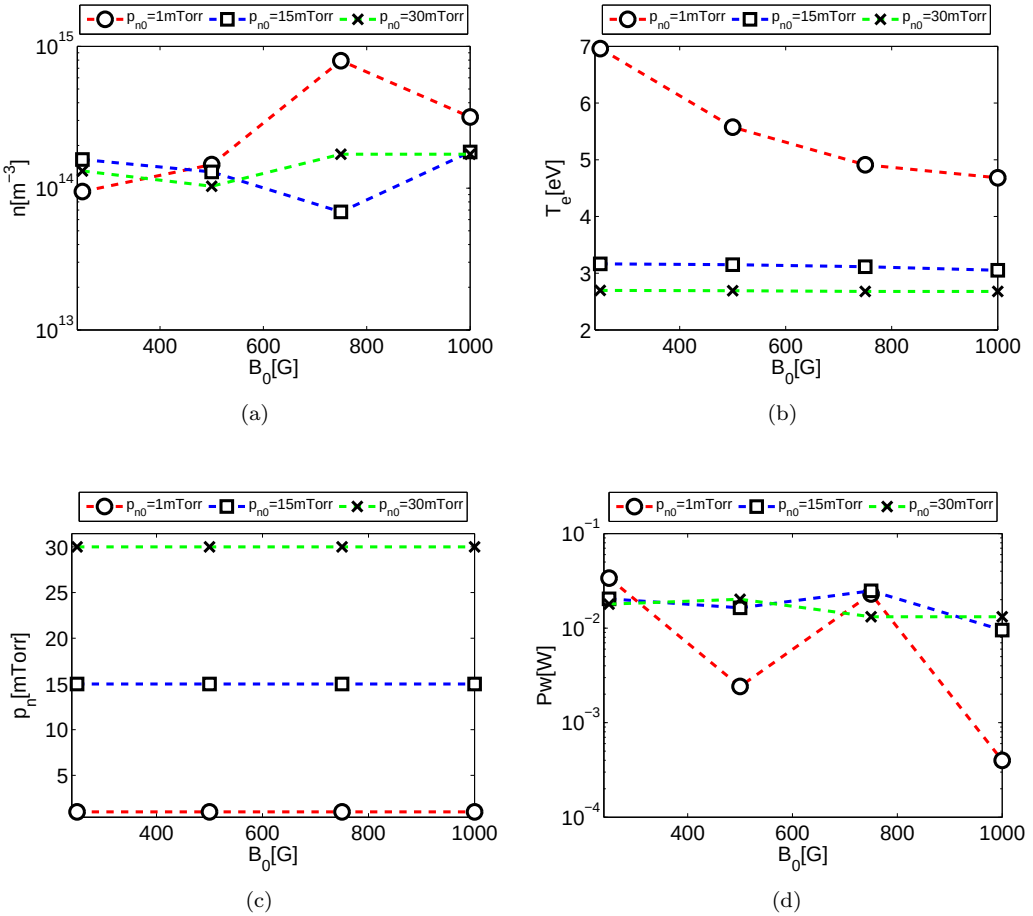

(a) (b)

(c) (d)

Figure 4.15: Equilibrium conditions in function of the quasi-axial magnetic field B_0: (a) plasma density, (b) electron temperature, (c) neutral pressure, (d) absorbed power. The plasma source is driven by a Fractional Helix antenna, which is fed by ΔV=100 V. We have analyzed p_{n0}=1 mTorr, p_{n0}=15 mTorr, p_{n0}=30 mTorr.

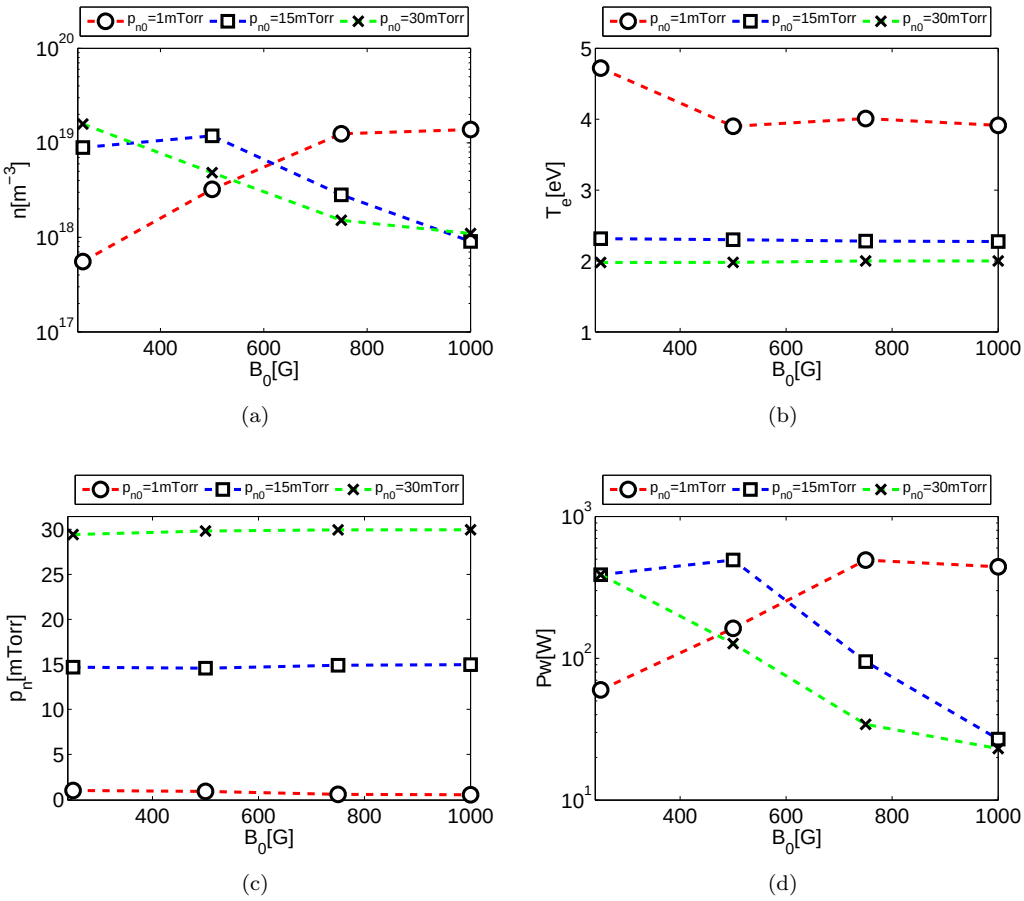

Figure 4.16: Equilibrium conditions in function of the quasi-axial magnetic field B_0: (a) plasma density, (b) electron temperature, (c) neutral pressure, (d) absorbed power. The plasma source is driven by a Fractional Helix antenna, which is fed by ΔV=500 V. We have analyzed p_{n0}=1 mTorr, p_{n0}=15 mTorr, p_{n0}=30 mTorr.

4.5 Antenna Analysis

Figs.4.17–19 shows the equilibrium configurations for different antennas, namely: Single-Loop, Nagoya type-III and Fractional Helix. In Figs.4.17–19 we have an overview of the working conditions that allows us to deposit the highest power within the plasma. Since we are interested in the propulsive space applications of the Helicon plasma sources, this analysis is necessary in order to optimize the propulsive figures of merit that are dependent on the power deposited. In Figs.4.17–19 are reported n, T_e, p_n and Pw at the equilibrium conditions against ΔV, respectively for *low values* of p_{n0} and B_0 (p_{n0}=1 mTorr, B_0=250 G in Fig.4.17), *medium values* (p_{n0}=15 mTorr, B_0=500 G in Fig.4.18), and *high values* (p_{n0}=30 mTorr, B_0=1000 G in Fig.4.19). In all the configurations it is possible to notice:

- a linear dependence of n from Pw;
- a decrease of p_n with the increase of Pw;
- a decrease of T_e with the increase of Pw, in particular T_e reaches the minimum value asymptotically and the maximum around the minimum value of Pw that allows the source to be sustained.

In the majority of the analyzed cases we have that increasing ΔV the power absorbed by the source increases, and consequently we have the variation of the other parameters. There is not an antenna that works better than the others in all the configurations: for *medium values* and *high values* of p_{n0} and B_0, and ΔV=100 V-250 V, the Single loop antenna works better than the others even thought it is the only one that is not able to sustain the plasma source for *low values* of B_0 and p_{n0}, and ΔV=100 V. The Pw trend is similar for the Nagoya type-III and the Fractional Helix for all the p_{n0}, B_0 analyzed; the trend of Pw with the Single Loop differs from that calculated with the other antennas (see Fig.4.17–19(d)).

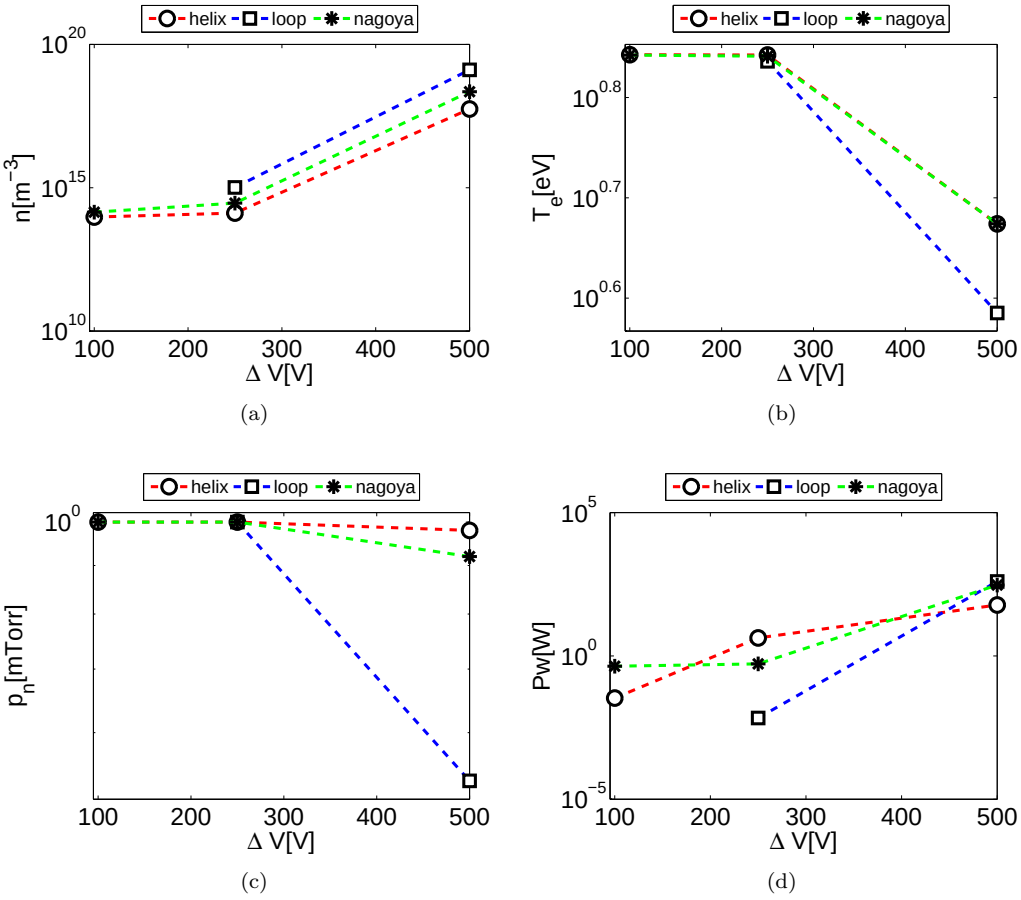

Figure 4.17: Equilibrium conditions in function of the voltage gap: (a) plasma density, (b) electron temperature, (c) neutral pressure, (d) absorbed power. The plasma source is driven by Single Loop, Nagoya Type-III, and Fractional Helix antennas. The input parameters are p_{n0}=1 mTorr, B_0=250 G.

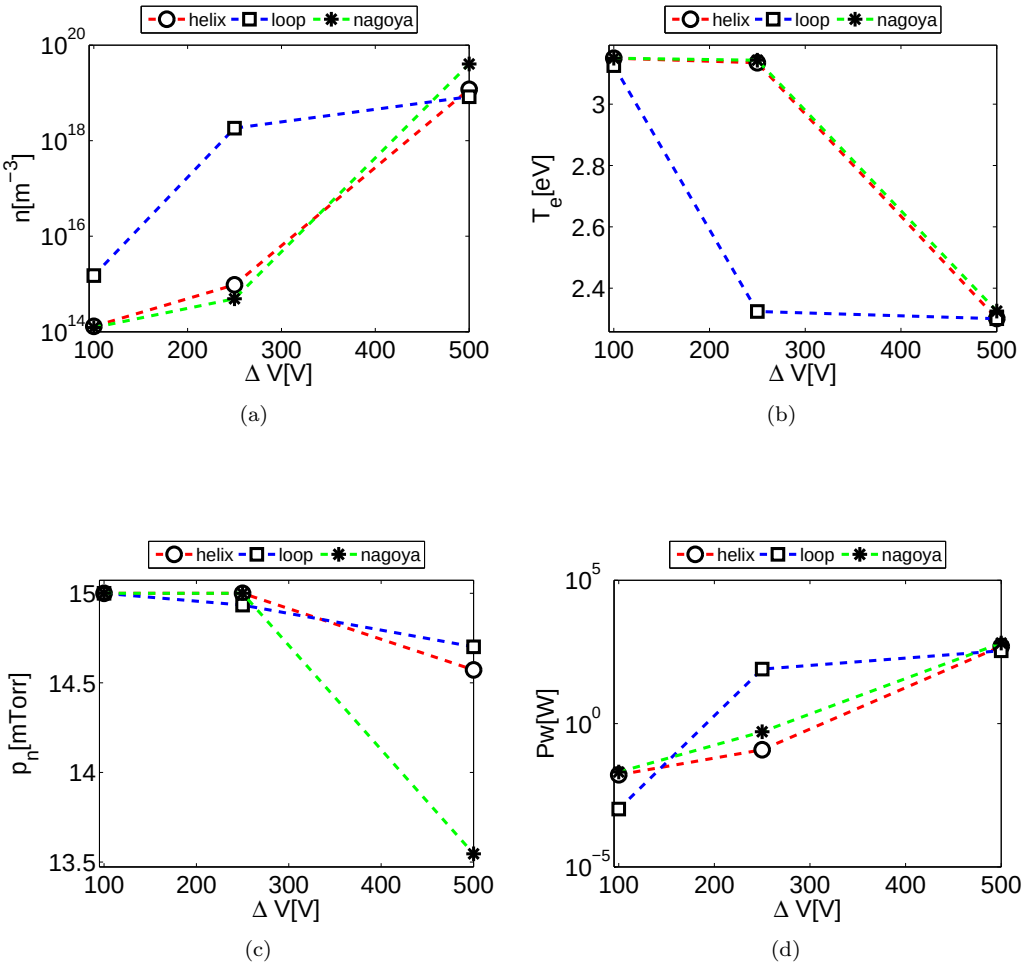

Figure 4.18: Equilibrium conditions in function of the voltage gap: (a) plasma density, (b) electron temperature, (c) neutral pressure, (d) absorbed power. The plasma source is driven by Single Loop, Nagoya Type-III, and Fractional Helix antennas. The input parameters are p_{n0}=15 mTorr, B_0=500 G.

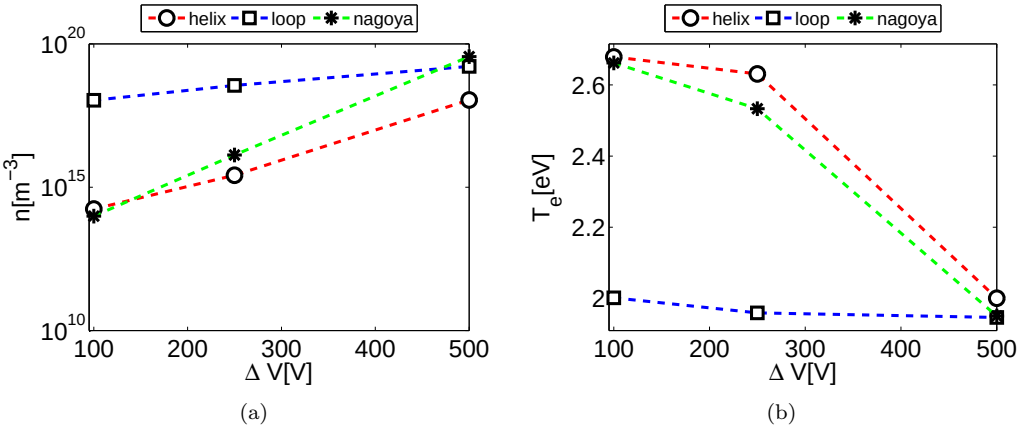

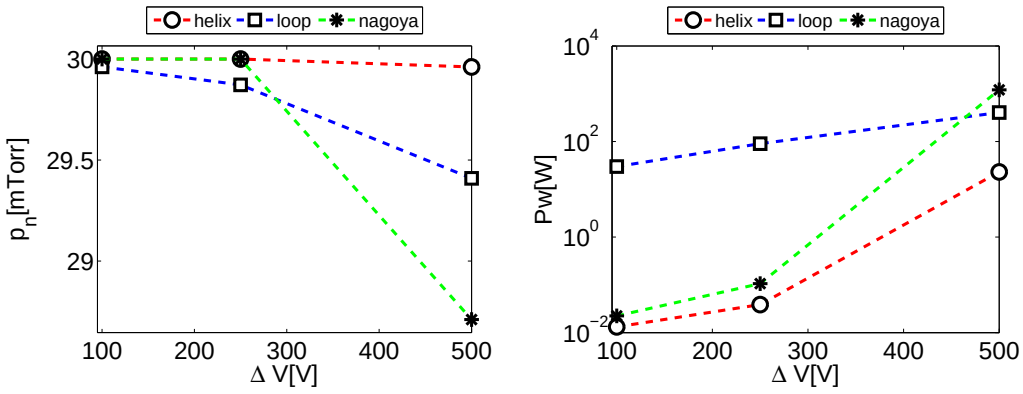

(c) (d)

Figure 4.19: Equilibrium conditions in function of the voltage gap: (a) plasma density, (b) electron temperature, (c) neutral pressure, (d) absorbed power. The plasma source is driven by Single Loop, Nagoya Type-III, and Fractional Helix antennas. The input parameters are p_{n0}=30 mTorr, B_0=1000 G.

4.5.1 Current Distribution

We have evaluated how the current density distribution varies during the iterative loops. In particular we focused on the influence that the plasma density n, which is not constant throughout the loop, has on the current density distribution. Also the electron temperature T_e and the neutral pressure p_n are loop variables, however in previous works it was shown that n has a major influence on the current density distribution than T_e and p_n [44]. The setup for our work is illustrated in Fig.4.2. We have chosen, for all the three geometrical configurations analyzed, a quasi-axial magneto-static field B_0=250 G, initial neutral pressure p_{n0}=15 mTorr, and a voltage gap ΔV=100 V. With those input values we have some of the wider variation of n, during the iterative loop, among the cases analyzed: n varies from three to five orders of magnitude depending on the geometry.

In Fig.4.20 we can see the current density distribution on the Single Loop antenna in the above mentioned case. In Fig.4.20(a) we have the first iteration of the loop when n is

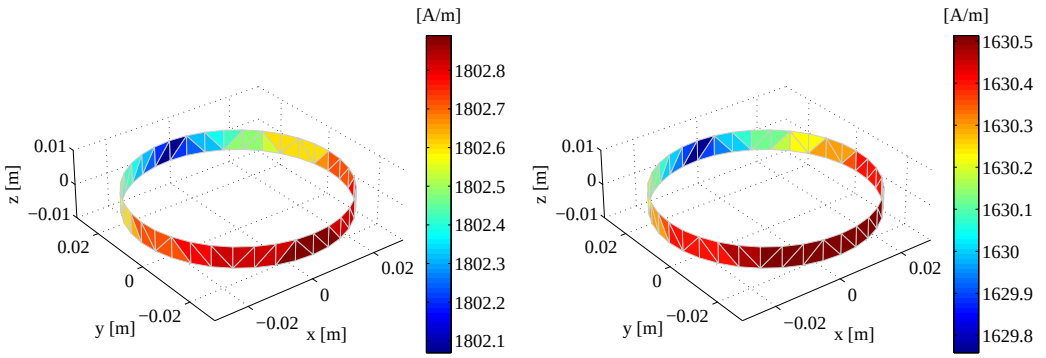

(a) (b)

Figure 4.20: Current density distribution on the surface of a Single Loop antenna: (a) in the first step of the convergence loop when $n \approx 10^{17}$ m^{-3}, (b) at the equilibrium when $n \approx 10^{14}$ m^{-3}. The input parameters are ΔV=100 V, B_0=250 G, p_{n0}=15 mTorr.

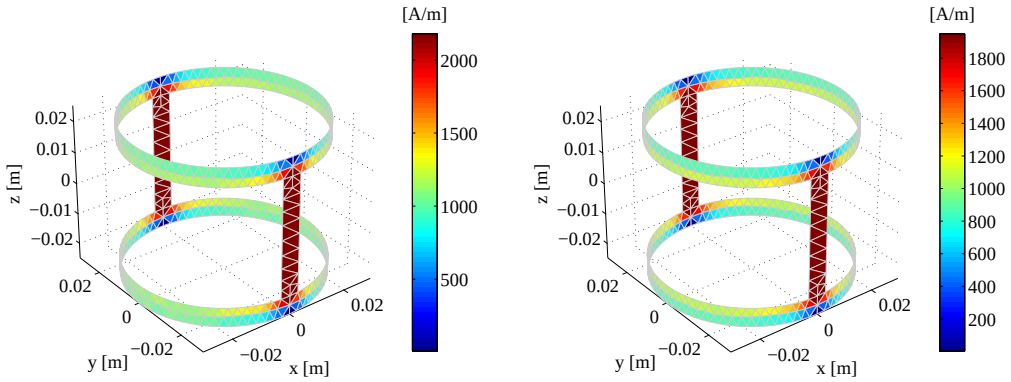

(a) (b)

Figure 4.21: Current density distribution on the surface of a Nagoya Type-III antenna: (a) in the first step of the convergence loop when $n \approx 10^{17}$ m^{-3}, (b) at the equilibrium when $n \approx 10^{14}$ m^{-3}. The input parameters are ΔV=100 V, B_0=250 G, p_{n0}=15 mTorr.

maximum ($n = 5.7 \times 10^{18}$ m^{-3}), and in 4.20(b) we have the last iteration of the loop when n is minimum ($n = 3.5 \times 10^{13}$ m^{-3}). The current density decreases with n however, even thought n varies of five orders of magnitude, the current density has a variation lower than the 10%. The pattern of the current density is not influenced by the variation of n.

In Fig.4.21 we can see the current density distribution on the Nagoya Type-III antenna in the above mentioned case. In Fig.4.21(a) we have the first iteration of the loop when n is maximum ($n = 5.7 \times 10^{18}$ m^{-3}), and in 4.21(b) we have the last iteration of the loop when n is minimum ($n = 1.6 \times 10^{14}$ m^{-3}). The current density decreases with n however, even thought n varies of four orders of magnitude, the current density has a variation lower than the 10%. The pattern of the current density is not influenced by the variation of n.

In Fig.4.22 we can see the current density distribution on the Fractional Helix antenna in the above mentioned case. In Fig.4.22(a) we have the first iteration of the loop when n is maximum ($n = 3.6 \times 10^{17}$ m^{-3}), and in 4.22(b) we have the last iteration of the loop when n is minimum ($n = 1.4 \times 10^{14}$ m^{-3}). The current density decreases with n however, even thought n varies of three orders of magnitude, the current density has a variation lower than the 2% b. The pattern of the current density is not influenced by the variation of n.

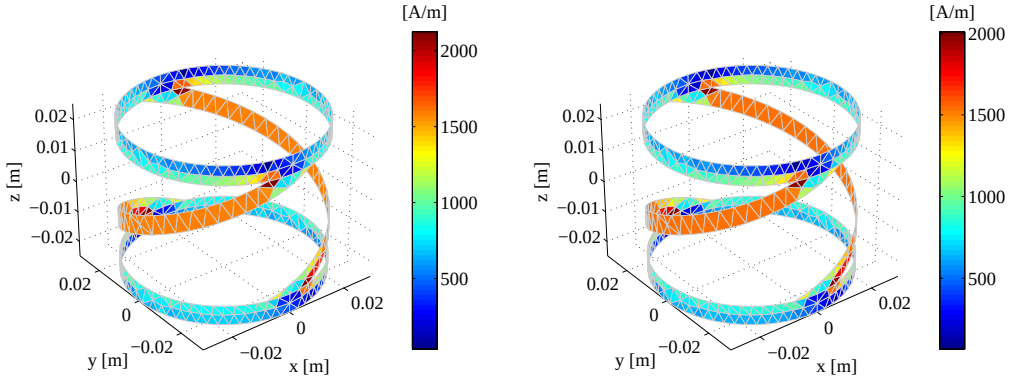

(a) (b)

Figure 4.22: Current density distribution on the surface of a Fractional Helix antenna: (a) in the first step of the convergence loop when $n \approx 10^{17}$ m^{-3}, (b) at the equilibrium when $n \approx 10^{14}$ m^{-3}. The input parameters are ΔV=100 V, B_0=250 G, p_{n0}=15 mTorr.

Chapter 5

Coupling ADAMANT and One-Dimensional Fluid Solver

The approach used to study the coupling of the wave propagation and the plasma transport in the 0-Dimensional model can be generalized in order to have a 1-D radial model of our plasma source. The electromagnetic problem, and the plasma dynamics will be solved separately and then coupled by means of an iterative loop. The input-output of respectively the electromagnetic solver and the fluid solver are the same of the 0-D model, but now they are radial profile and not only mean values. For the electromagnetic solver: (i)the input are the radial plasma parameters profiles, e.g. radial plasma density profile, (ii) the output is the deposited power profile. For the fluid solver: (i)the input is the deposited power profiles, (ii) the output are the plasma parameters profile. This approach is justified because in the study of the plasma transport, the wave propagation can be retained as a source term through the power deposited by the antenna into the plasma; in the solution of wave propagation the plasma parameters can be considered as stationary. In this chapter we present the results obtained coupling the ADAMANT code, that solves for the electromagnetic coupling between the antenna and the plasma discharge, with a one-dimensional fluid code that solves for the radial profiles values of the plasma density, electron temperature, and neutral pressure within the discharge.

The profiles of plasma density (n), electron temperature (T_e), neutral pressure(p_n), and power absorbed by the plasma discharge (Pw_r) are the parameters considered to evaluate the equilibrium conditions of the source. In our model we do not consider outflows. We have investigated three different antennas, namely: the Single Loop, the Nagoya type III, and the Fractional Helix as previously done in the 0-D model (see Fig.4.2). These antennas are all coupled to a plasma cylinder with identical geometry of that used in the 0-D analysis. Also the plasma cylinder and the antennas are meshed as in the 0-D model presented in Chapter 4, in fact: (i)the antenna mesh is in agreement with the criterion of λ_0 discussed in Chapter 3; (ii) the plasma mesh used in coupling ADAMANT and GlobalModel samples the EM fields accurately enough to be employed in a 1D model, as shown in Chapter 3. The parameters considered in this study are: the magneto-static field (B_0), the initial neutral background pressure(p_{n0}), the voltage gap that drives the antenna(ΔV). All the antennas work at a frequency of 13.56 MHz. We can calculate the total power deposited in the source through the integration of Pw_r:

$$Pw = 2\pi \int_0^b Pw_r r dr \tag{5.1}$$

5.1 Iterative Loop

We are going to give a quick description of the iterative loop to couple ADAMANT and the 1-D fluid solver. The input of the iterative loop are the geometry of the source, p_{n0}, B_0, ΔV, and the working frequency that drives the antenna; the output are n, p_n, T_e and Pw_r profiles. n, p_n, T_e are the solution of the plasma transport, and Pw_r is the solution of the EM problem; however n, p_n, T_e are output of the fluid solver while Pw_r has to be calculated from the ADAMANT output.

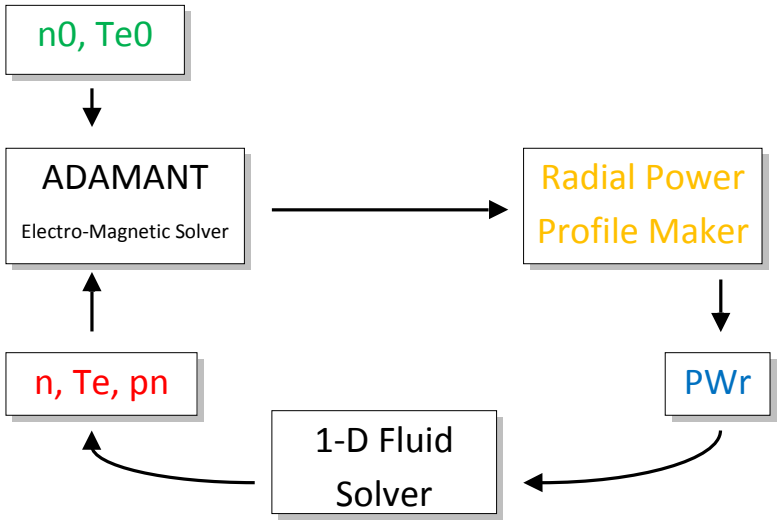

Figure 5.1: Sketch of the iterative loop.

In our model (see Fig.5.1) ADAMANT runs first, it is initialized with a first guess n_0 and T_{e0}; specifically n_0 and T_{e0} are radial profiles supposed constant. The input of ADAMANT are n, p_n, and T_e profiles; the Radial Power Profile Maker evaluates the Pw_r profile from the ADAMANT output file *adamant_DIELECTRC_D.txt* (see Chapter 2). Pw_r is the input profile of the 1-D fluid solver which provides n, p_n, T_e; with those updated profiles the loop restarts, and so on until the convergence is reached. The convergence criterion implemented is: the relative error between two consecutive steps must be lower than a threshold value.

More specifically the Radial Power Profile Maker works in this way: the ADAMANT output provides the electric flux density related to the SWGs (see Appendix B) built on the unstructured mesh of ADAMANT. From this information it is possible to calculate the power deposited into each tetrahedron of the plasma mesh, but to obtain Pw_r it is necessary to sample this deposited power in a radial structured mesh (see Section 3.2.1). In order to avoid the introduction of numerical noise in this operation we have done a preliminary mesh analysis on both the unstructured and the structured mesh (see Section 3.2.2).

5.2 Data

We have analyzed a plasma source where the quasi-axial magnetic field is B_0=250 G, the initial neutral background pressure is p_{n0}=30 mTorr and the antenna is fed by a voltage gap ΔV=500 V. In particular we have compared the equilibrium conditions reached when the source is driven by three different antennas, namely: Single Loop, Nagoya Type-III, and Fractional Helix.

5.2.1 Single Loop Antenna

When the source is driven by a Single Loop antenna the radial profiles of the loop variables are represented in Fig.5.2. In this case we can see a particularly fast convergence of the iterative loop: also in the second iteration step the difference between the actual profiles (labeled *Run*2 in Fig.5.2) and the equilibrium profiles (labeled *Run*4 in Fig.5.2) is in the order of 1%.

The Pw_r profile has a peak in the region near the outer edge of the plasma cylinder (see Fig.5.2(d)); this phenomenon is due to the contribution of the TG waves, in fact the mechanism of power deposition that involves those waves is mainly concentrate near the outer edge of the plasma cylinder [19]. Near the outer edge we have that n has a minimum (see Fig.5.2(a)) and p_n has a peak (see Fig.5.2(c)); the plasma density is peaked in the center of the plasma cylinder even thought the majority of the power is deposited near the outer edge because of the contribution of the plasma transport [33]. T_e is almost constant along the radius of the plasma cylinder, more precisely a low amplitude peak is noticed near the outer edge (see Fig.5.2(b)).

A week difference can be found by comparing: (i)the average values of n, p_n, T_e and the global power absorbed by the source Pw calculated coupling ADAMANT and GlobalModel (see Fig.4.6),(ii) and those obtained integrating the radial profiles calculated coupling ADAMANT and the 1-D fluid solver.

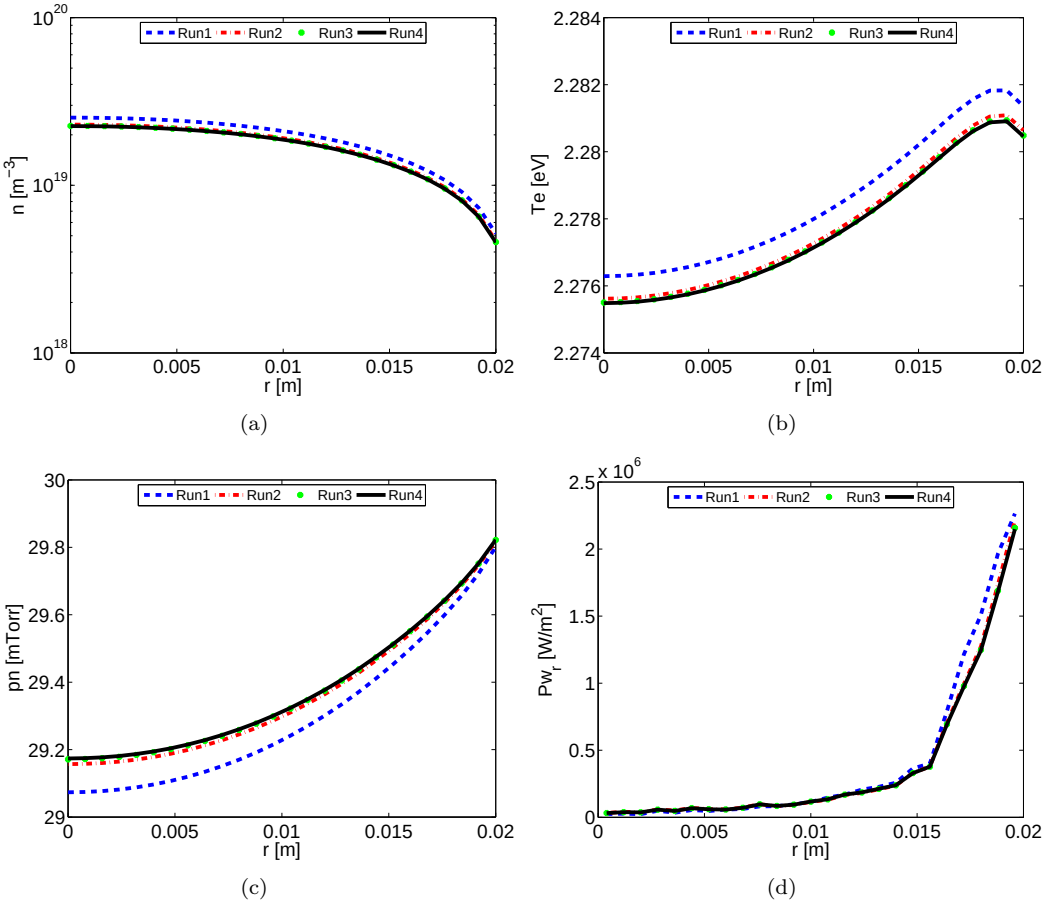

Figure 5.2: Radial profiles evolution during the convergence loop: (a) plasma density, (b) electron temperature, (c) neutral pressure, (d) absorbed power. The plasma source is driven by a Single Loop antenna fed by ΔV=500 V. The input values are p_{n0}=30 mTorr, B_0=250 G.

5.2.2 Nagoya Type-III Antenna

When the source is driven by a Nagoya Type-III antenna the radial profiles of the loop variables (e.g. plasma density n, and deposited power Pw_r) are represented in Fig.5.3. In this case we can see a particularly fast convergence of the iterative loop: also in the third iteration step the difference between the actual profiles (labeled $Run3$ in Fig.5.3) and the equilibrium profiles (labeled $Run4$ in Fig.5.3) is in the order of 1%.

The plasma parameters profiles has the same trend of those calculated with the Single Loop antenna: the Pw_r profile has a peak in the region near the outer edge of the plasma cylinder (see Fig.5.3(d)); near the outer edge we have that n has a minimum (see Fig.5.3(a)) and p_n has a peak (see Fig.5.3(c)); T_e is almost constant along the radius of the plasma cylinder(see Fig.5.3(d)). A week difference can be found by comparing the results of ADAMANT coupled with GlobalModel, and the mean values obtained through the integration of the profiles calculated coupling ADAMANT and the 1-D fluid solver.

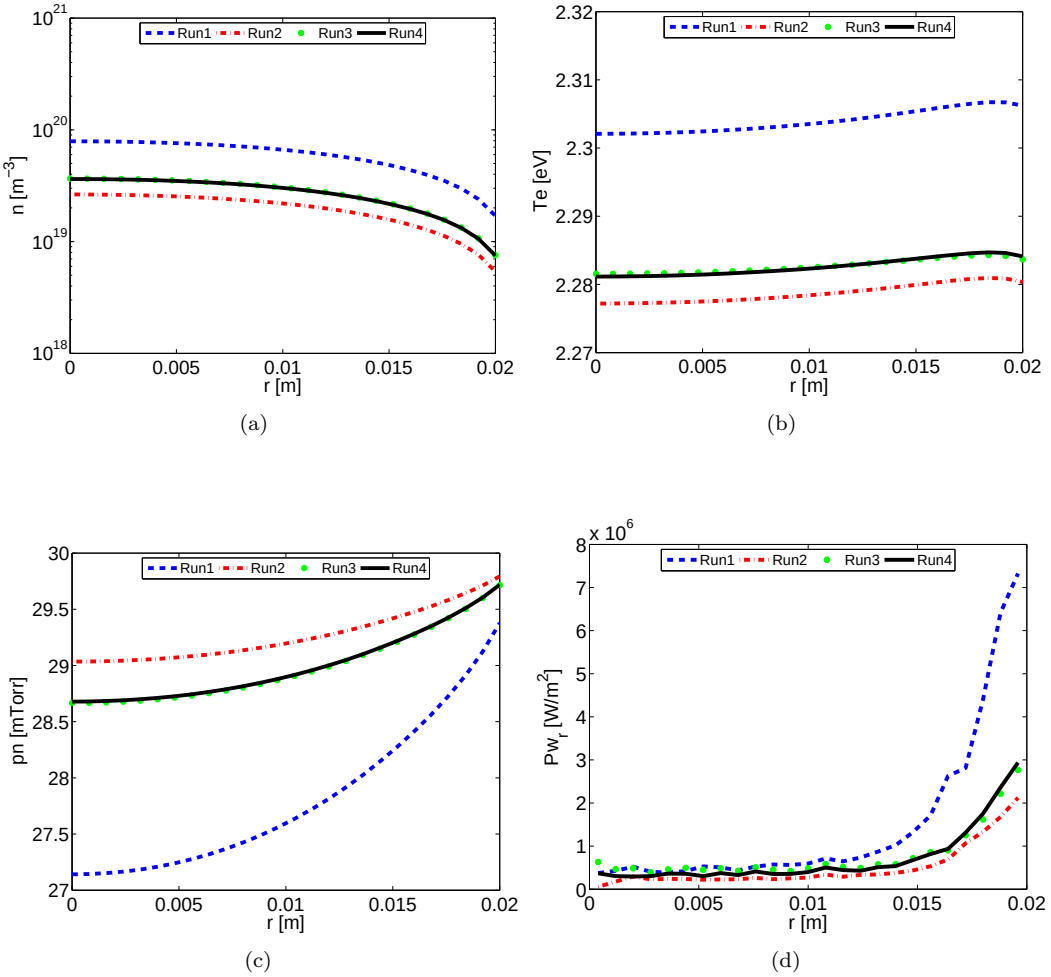

Figure 5.3: Radial profiles evolution during the convergence loop: (a) plasma density, (b) electron temperature, (c) neutral pressure, (d) absorbed power. The plasma source is driven by a Nagoya Type-III antenna fed by ΔV=500 V. The input values are p_{n0}=30 mTorr, B_0=250 G.

5.2.3 Fractional Helix Antenna

When the source is driven by a Fractional Helix antenna the radial profiles of the loop variables (e.g. plasma density n, and deposited power Pw_r) are represented in Fig.5.4. In this case we can see a particularly fast convergence of the iterative loop: also in the third iteration step the difference between the actual profiles (labeled $Run3$ in Fig.5.4) and the equilibrium profiles (labeled $Run4$ in Fig.5.4) is in the order of 2%.

The plasma parameters profiles has the same trend of those calculated with the other antennas: the Pw_r profile has a peak in the region near the outer edge of the plasma cylinder (see Fig.5.3(d)); near the outer edge we have that n has a minimum (see Fig.5.3(a)) and p_n has a peak (see Fig.5.3(c)); T_e is almost constant along the radius of the plasma cylinder(see Fig.5.3(d)). A week difference can be found by comparing the results of ADAMANT coupled with GlobalModel, and the mean values obtained through the integration of the profiles calculated coupling ADAMANT and the 1-D fluid solver.

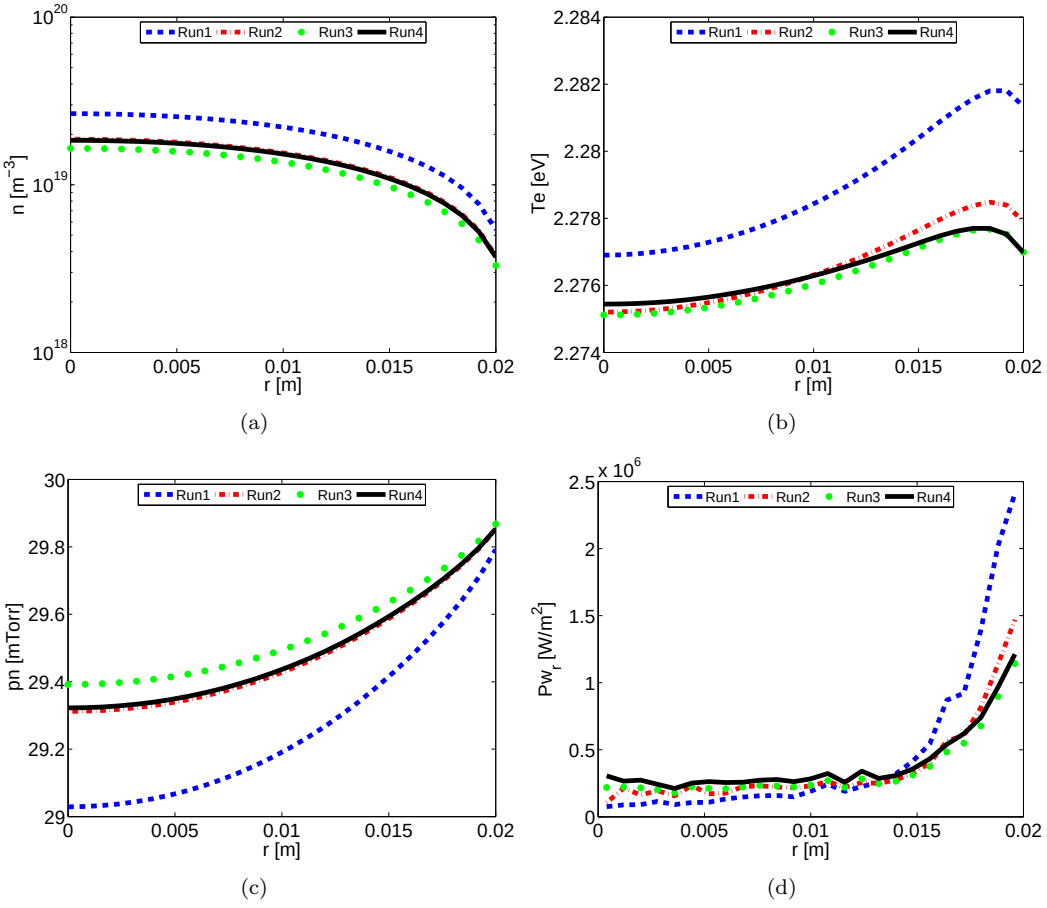

Figure 5.4: Radial profiles evolution during the convergence loop: (a) plasma density, (b) electron temperature, (c) neutral pressure, (d) absorbed power. The plasma source is driven by a Fractional Helix antenna fed by ΔV=500 V. The input values are p_{n0}=30 mTorr, B_0=250 G.

5.2.4 Antenna Analysis

In Fig.5.5 we have the comparison between the equilibrium conditions reached in the three different geometrical configurations analyzed in the previous sections; the input parameters are: B_0=250 G, p_{n0}=30 mTorr, ΔV=500 V.

In all the three analyzed cases we have: (i) a peak of Pw_r near the outer edge of the plasma cylinder (see 5.5(d)), (ii) a minimum of n near the outer edge (see 5.5(a)), (iii) T_e approximately constant in the radial direction (see 5.5(b)). In Fig.5.5(d) we can see that the antenna geometry affects the absorbed power profile (e.g. the ratio between the maximum and the minimum values of Pw_r is greater when the source is driven by a Single Loop antenna than by a Fractional Helix). On the contrary the antenna geometry influence the average value of n and the p_n, but not the shape of their profiles (see Fig.5.5(a) and Fig.5.5(c)). T_e is not very influenced by the antenna geometry in the analyzed cases (see Fig.5.5(b)).

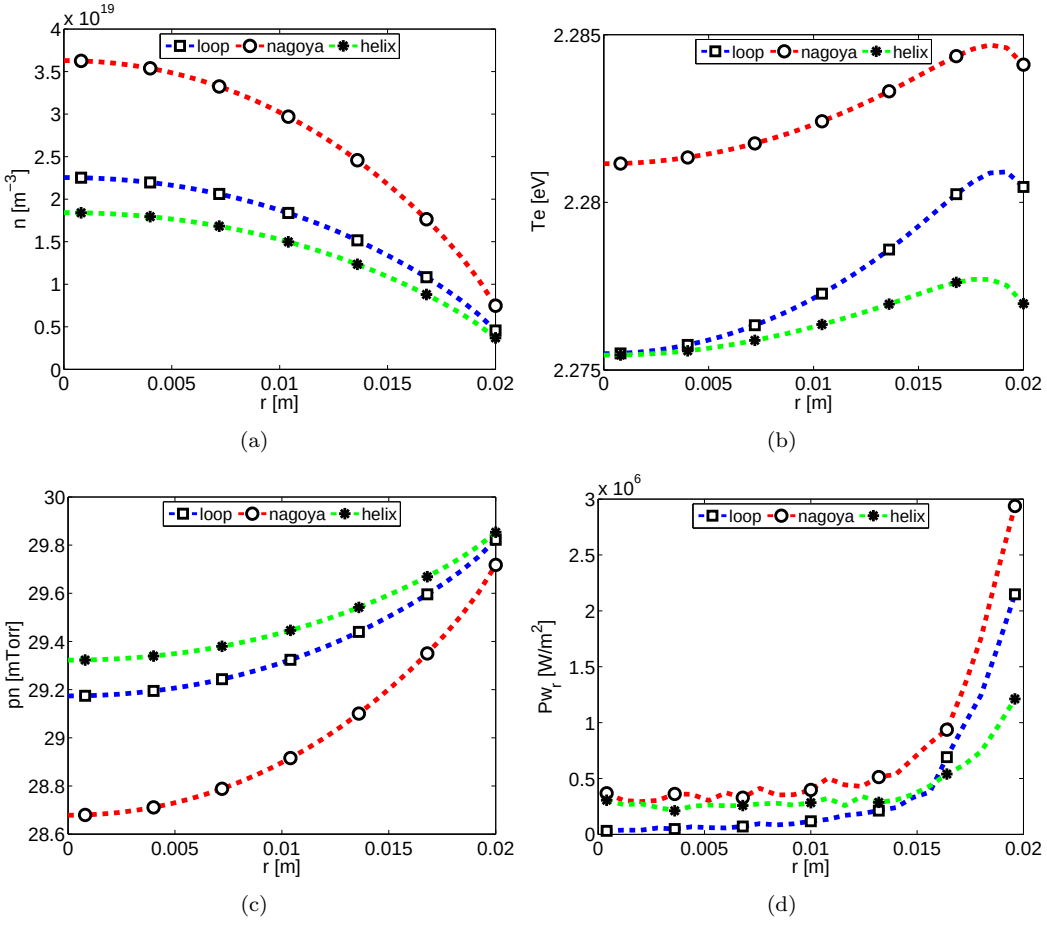

Figure 5.5: Radial profiles at the equilibrium conditions: (a) plasma density, (b) electron temperature, (c) neutral pressure, (d) absorbed power. The plasma source is driven by Single Loop, Nagoya Type-III, and Fractional Helix antennas. The input parameters are: ΔV=500 V, p_{n0}=30 mTorr, B_0=250 G.

Chapter 6

Conclusions

In HPTs the propulsive figures of merit (such as specific impulse and thrust) are connected to the plasma parameters (i.e. plasma density and temperature) that in turn are related to the power transferred to the plasma. We have focused our attention on the high-power (> 1 kW) Helicon plasma sources because powers of this order of magnitude will be employed in many devices that are now under development (such as in the HPT that will be realized in the SAPERE project).

In an Helicon plasma source the power deposition is affected by: (i) antenna-plasma coupling, (ii) wave propagation, and (iii) plasma transport. Standard approaches rely on electromagnetic simulations coupled to either fluid or kinetic or PIC strategies to reproduce the plasma response. However the modeling of high-power Helicon sources, where high values of the plasma density can be achieved (also up to 10^{19} m^{-3}), would result in long simulation time and huge computational costs in a kinetic or PIC approach. In our case the best trade off between accuracy and computational cost is obtained with a fluid model that reproduces the plasma motion.

To model the coupling of the wave propagation and the plasma transport in such a source we have studied separately the electromagnetic and plasma dynamics phenomena. These phenomena had been solved by means of an electromagnetic and a fluid solver, respectively, whereas both solvers had been coupled through an iterative loop. In this loop the output of the electromagnetic solver (the power deposited into the plasma) is the input of the fluid solver that solves for the plasma transport. Similarly, the output quantities of the fluid solver, e.g. plasma density and electron temperature, are the input for the electromagnetic solver. The ADAMANT code that solves for the electromagnetic coupling between the antenna and the plasma discharge had been respectively coupled with two fluid solvers in order to have: (i) a 0-D model of the source; (ii) a 1-D radial model of the source.

The accuracy of the solution and the computational cost are related to the number of elements in which both the antenna and the plasma cylinder are discretized, in fact those are related to the basis functions used in the simulation. A mesh analysis has been performed in order to find the best trade off between accuracy and calculation time. We paid particular attention in the coupling of ADAMANT with the 1-D fluid solver: in order to calculate the radial power profile we must sample on a structured radial mesh the local power deposited (calculated by ADAMANT); specifically, the number of radial nodes is to be chosen in such a way to avoid numerical noise. The radial power profile calculated from ADAMANT output has been benchmarked against the results of SPIREs, another well established numerical tool specifically conceived to evaluate the radial power deposition profile in magnetized plasma waveguides.

The output of the numerical solver obtained coupling ADAMANT and respectively the 0-D and 1-D fluid solver are the equilibrium values of: plasma density (n), electron temperature (T_e), neutral pressure(p_n), and power absorbed by the source(Pw). We have investigated three different antennas, namely: the Single Loop, the Nagoya type III, the Fractional Helix.

The input parameters investigated in this study are: (i) the magneto-static field (B_0), from 250 G to 1000 G; (ii) the initial neutral background pressure(p_{n0}), from 1 mTorr to 30 mTorr; (iii) the voltage that drives the antenna(ΔV), from 100 V to 500 V.

In most cases we have that Pw increases withΔV. As a rule of thumbs: (i) in general Pw increases with B_0; (ii) none remarkable effects on Pw is noticed varying p_{n0}, but Te decreases if p_{n0} increases. Broadly speaking there is not an antenna geometry that performs better than the others in all the configurations analyzed; the antenna shape affects the equilibrium parameters of the plasma discharge. There is a strong correlation between the equilibrium parameters: (i) n depends linearly from Pw; (ii) p_n and T_e decrease if Pw increases.

We have analyzed also the variation of the current density distribution during the iterative loop. The current density is quite independent on T_e and p_n, and it has the same trend of n; however the greatest variation of the current density, in the order of 10%, is associated with a variation of five orders of magnitude in the plasma density. The pattern of the current density is invariant during the iterative loop.

We have calculated a 1-D radial equilibrium configuration for the three antennas and for B_0=250 G, p_{n0}=30 mTorr and ΔV=500 V. In all the three analyzed cases we have: (i) a peak of the deposited power profile near the outer edge of the plasma cylinder; (ii) a minimum of n near the outer edge; (iii) T_e approximately constant in the radial direction. In particular we have: (i) the peak of the deposited power profile near the edge is chiefly due to the contribution of the TG waves, in fact the mechanism of power deposition that involves those waves is mainly concentrate near the outer edge of the plasma cylinder; (ii) the plasma density is peaked in the center of the plasma cylinder even thought the majority of the power is deposited near the outer edge because of the contribution of the plasma transport. The antenna geometry affects the absorbed power profile; on the contrary, the antenna geometry influences the average value of n and the p_n, but not the shape of their profiles. T_e is not influenced by the antenna geometry in the analyzed cases.

Appendix A

The Rao-Wilton-Glisson Basis Function

The expression of the n-th RWG basis function defined on two adjoining triangles T_n^+ and T_n^- connected through the n-th common edge is [45]

$$\mathbf{f_n}(\mathbf{r}) = \begin{cases} \frac{l_n}{2A_n^+}\rho_{\mathbf{n}}^+ & \mathbf{r} \in T_n^+ \\ \\ \frac{l_n}{2A_n^-}\rho_{\mathbf{n}}^- & \mathbf{r} \in T_n^- \end{cases} \tag{A.1}$$

where $\rho_{\mathbf{n}}^{\pm}$ are the position vectors with respect to triangular vertexes $O_n^{\pm}$, $\mathbf{r}$ is the position vector with respect to the global origin O, $A_n^{\pm}$ is the area of triangle $T_n^{\pm}$, and l_n is the length of the common edge, as shown in Figs. A.1(a), (b).

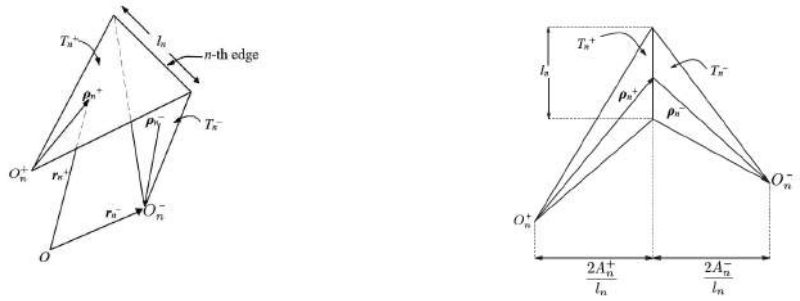

(a) (b)

Figure A.1: Geometrical parameters associated with the n-th RWG basis function, with (a) triangle pair and geometrical parameters associated with interior edge, and (b) geometry for construction of component of basis function normal to the edge.

The basis function $\mathbf{f_n}$ is used to approximately represent the surface current, and some of its properties are:

1. The normal component of the current is continuous across the common edge, and the current component normal to the boundary of the surface formed by $T_n^+ \cup T_n^-$ is zero. Consequently, no line charges are present along the common (interior) edge and along the outer boundary of the RWG function. Moreover the surface divergence in $T_n^{\pm}$ of $\mathbf{f_n}$ is proportional to the surface charge density associated with the triangular patch,

and it is

$$\nabla_S \cdot \mathbf{f_n}(\mathbf{r}) = \begin{cases} \frac{l_n}{A_n^+} & \mathbf{r} \in T_n^+ \\ \frac{l_n}{A_n^-} & \mathbf{r} \in T_n^- \\ 0 & \text{otherwise} \end{cases} \tag{A.2}$$

We can conclude that the surface charge density is constant within a single triangle, and the total charge associated with the triangle pair $T_n^{\pm}$ is zero.

2. The normal component on the boundary of $T_n^+ \cup T_n^-$ is zero.

We can approximate the current on the metal surface in terms of the $\mathbf{f_n}$ as

$$\mathbf{J_A} \cong \sum_{n=1}^{N} I_n \mathbf{f_n}(\mathbf{r}) \tag{A.3}$$

where N is the number of interior (non boundary) edges. Each non boundary edge of the mesh is associated with a basis function, so up to three basis functions may have nonzero values within each triangular patch. Moreover, at a given edge only the basis function associated with that edge has a nonzero current component normal to the edge, since all other basis functions in adjacent patches are parallel to the edge.

Appendix B

The Schaubert-Wilton-Glisson Basis Function

The expression of the p-th SWG basis function defined on two adjoining tetrahedrons Ω_p^+ and Ω_p^- connected through the p-th shared facet is [46]:

$$\mathbf{v_p}(\mathbf{r}) = \begin{cases} \frac{A_{4p}}{3V_p^+}\rho_{\mathbf{n}}^+ & \mathbf{r} \in \Omega_n^+ \\ \\ \frac{A_{4p}}{3V_p^-}\rho_{\mathbf{n}}^- & \mathbf{r} \in \Omega_n^- \end{cases} \tag{B.1}$$

where A_{4p} represents the area of the shared facet, $V_p^{\pm}$ are the volumes of $\Omega_p^{\pm}$, $\rho_{\mathbf{p}}^{\pm}$ are the position vectors with respect to tetrahedral vertexes $O_p^{\pm}$, and $\mathbf{r}$ is the position vector with respect to the global origin O, as shown in Fig.B.1. The basis function $\mathbf{v_p}$ is used to

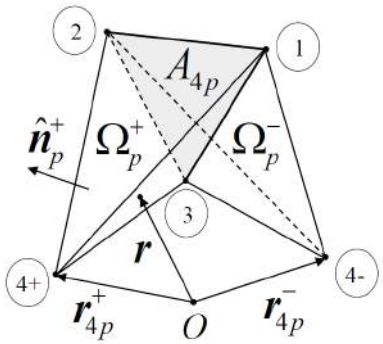

Figure B.1: Tetrahedron pair and geometrical parameters associated with the p-th SWG basis function

approximately represent the electric flux density, and some of its properties are

1. $\mathbf{v_p}$ has the normal component to any face equal to zero except for the shared facet of the tetrahedral pair $O_p^{\pm}$, which is constant and continuous across the facet;
2. if the p-th facet belongs to the boundary surface S_p of the plasma volume V_p , $\mathbf{v_p}$ may

have support just on tetrahedron Ω_p^+:

$$\mathbf{v_p}(\mathbf{r}) = \begin{cases} \frac{A_{4p}}{3V_p^+}\rho_{\mathbf{n}}^+ & \mathbf{r} \in \Omega_n^+ \\ \\ 0 & \text{otherwise} \end{cases} \tag{B.2}$$

The latter type of functions is required to account for the physical fact that $\mathbf{D}_P \cdot \hat{\mathbf{n}}$ is nonzero on S_P.

We can approximate the total electric flux density in the plasma volume in terms of the $\mathbf{v_p}$ as

$$\mathbf{D_P} \cong \sum_{p=1}^{N_P} D_p \mathbf{v_p}(\mathbf{r}) \tag{B.3}$$

Bibliography

[1] F. F. Chen and D. Arnush, *Generalized theory of helicon waves I. Normal modes*, Phys. Plasmas, Vol. 4, No. 9, 3411–3421, 1997.

[2] Y. Mouzouris and J. E. Scharer, *Modeling of profile effects for inductive Helicon plasma sources*, IEEE Transactions on Plasma Science, vol. 24, no. 1, 1996.

[3] B. Beal and F. Mak, *Operating characteristics of cylindrical and annular helicon sources*, IEPC, September 2007.

[4] J. M. Pucci, *An analysis of energy balance in a helicon plasma source for space propulsion*, Ph.D. dissertation, Arizona State University, 2003.

[5] S. H. Kim and Y. Hwang, *Collisional power absorption near mode conversion surface in helicon plasmas*, Plasma phys. Control. Fusion, vol. 50, 2008.

[6] F. F. Chen, I. D. Sudit, and M. Light, *Plasma Sources*, Science Technology, vol.5, 474-491, 1996.

[7] R. Gallet, J. M. Richardson, B. Wieder, and G. D. Ward, *Microwave whistler mode propagation in a dense laboratory plasma*, Phys. Rev. Lett., vol. 4, 1960.

[8] H. Blevin and P. Thonemann, Culham Laboratory, *Tech. Rep. CLMR66*, 1966.

[9] J. Lehane and P. Thonemann, *An experimental study of helicon wave propagation in a gaseous plasma*, Proc. Phys. Soc., 1965.

[10] R. Boswell, *Modulated RF produced argon magneto-plasma*, School of Physical Sciences, Finders University, Australia, Tech. Rep. PR. 68/8,1968.

[11] T.H.Stix, *Theory of Plasma Waves*. McGraw-Hill, 1962.

[12] S. O. Knox, F. Paoloni, and Kristiansen, *Helical antenna for exciting azimuthally asymmetric alfven waves*, M. J. Appl. Phys., 1975.

[13] T. Watari, T. Hatori, R. Kumasawa, S. Hidekuma et al., *Radio-frequency plugging of a high density plasma*, Phys. Fluids, 1978.

[14] R. Boswell, R. Porteous, A. Prytz, and A. Bouchoule, *Some features of RF excited fully ionised low pressure argon plasma*, Phys. Letts. A., 1982.

[15] F. F. Chen, *Physics of helicon discharges*, Electrical Engeneering Department, University of California, Los Angeles, California, Tech. Rep.

[16] H. A. Blevin and P. Christiansen, *Propagation of Helicon waves in a non-uniform plasma*, Aust. J. Phys., vol. 19, no. 501, 1966.

[17] A. W. Trivelpiece and R. W. Gould, *Appl. Phys.*, vol. 30, 1959.

[18] F.F.Chen and D.Arnush, *Generalized theory of helicon waves II. Excitation and absorption*, Phys. Plasmas, Vol. 5, 1239, 1998.

[19] D.Arnush, *The role of Trivelpiece-Gould waves in antenna coupling to helicon waves*, Phys. Plasmas 7 (7) (2000) 3042–3050.

[20] F. F. Chen, *Plasma ionization by helicon waves*, Plasma Physics Controlled Fusion, vol. 33, no. 339, 1991.

[21] F. F. Chen and D. D. Blackwell, *Upper Limit to Landau Damping in Helicon Discharges*, 1998.

[22] Y. Mouzouris and J. Scharer, *Two-dimensional (r,z) plasma wave absorption and poynting flux simulations for Helicon Sources*, IEEE Transactions on Plasma Science, vol. 27, no. 1, February 1999.

[23] D. Arnush, *The role of Trivelpiece-Gould waves in antenna coupling to helicon waves*, 2000.

[24] D. Melazzi, D. Curreli, M.Manente, J. Carlsson, and D. Pavarin, *SPIREs: A Finite-Difference Frequency-Domain electromagnetic solver for inhomogeneous plasma cylinders*, Computer Physics Communications, vol.183, No. 6, 1182–1191, 2012.

[25] D. Melazzi and V. Lancellotti, *ADAMANT: A surface and volume integral-equation solver for the analysis and design of helicon plasma sources*, February 2014.

[26] Birdsall C.K. and Langdon A.B., *Plasma Physics via Computer Simulation*, Adam Hilger Bristol, Philadelphia and New York, 1991.

[27] Lapenta G., *Particle In Cell Methods With Application to Simulations in Space weather*, Centrum voor Plasma Astrofysica, Katholieke Universiteit Leuven.

[28] Dawson J. M., *Particle simulation of plasmas*, Mod. Phys. No. 2, 1983.

[29] Beig R., Domcke W., et al., *Computational Many-Particle Physics Lecture Notes in Physics*, Springer, 2007.

[30] Hockney R. W. and Eastwood J.W., *Computer Simulation Using Particles*, Adam Hilger Bristol, Philadelphia and New York, 1988.

[31] Chen F.F., *Introduction to Plasma Physics and Controlled Fusion, vol.1*, 2nd Edition, Springer, New York, 2006.

[32] D. Curreli, D. Melazzi, M.Manente, D.Pavarin, *Equilibrium Conditions of Radiofrequency-heated Plasma Cylinders*, Progress In Electromagnetics Research Symposium Proceedings, Moscow, Russia, August 19–23, 2012

[33] D. Curreli, F. F. Chen, *Equilibrium theory of cylindrical discharges with special application to Helicons*, Phys. Plasmas, Vol. 18, pp.113–501, 2011.

[34] D. Bose, T. R. Govindan, and M. Meyyappan, *Modeling of a Helicon Plasma Source*, IEEE Transactions on Plasma Science, vol. 31, no. 4, August 2003

[35] D. Bose, T. R. Govindan, and M. Meyyappan, *A continuum model for the inductively coupled plasma reactor in semiconductor processing*, J. Electrochem. Soc., vol. 146, pp. 2705–2711, 1999.

[36] D. Pavarin, *et al.*, *Development of plasma codes for the design of minihelicon thrusters*, in 32nd International Electric Propulsion Conference, Wiesbaden, Germany, September 2011.

[37] E.Ahedo, *Plasmas for space propulsion*, Plasma phys. Control. Fusion, vol. 53.

[38] D. Pavarin, F. Ferri, and M. Manente, *Helicon plasma hydrazine.combined micro*, in XX AIDAA Congress, Milan, Italy, 2009.

[39] D. Pavarin et al., *Helicon Plasma Hydrazine.COmbined Micro project overview and development status*, in Proceedings of Space Propulsion Conference, San Sebastian, Spain, 2010.

[40] SAPERE, *Space Advanced Project for Excellence in Research and Enterprise*

[41] R. Harrington, *Field Computation by Moment Method*, New York, 1968.

[42] C. Geuzaine and J. Remacle, *GMSH: a three-dimensional finite element mesh generator with built-in pre- and post-processing facilities.*

[43] G. Zilli, *Calcolo Numerico*, Libreria Progetto, Padova, 2011.

[44] D.Melazzi and V.Lancellotti, *A comparative study of radiofrequency antennas for Helicon plasma sources*, Plasma Sources Sci. Technol. 24 (2015) 025024.

[45] S. Rao, D. Wilton, and A. Glisson, *Electromagnetic scattering by surfaces of arbitrary shape*, IEEE Trans. on Antennas and Propagation, vol. 30, pp. 409–418, 1982.

[46] D. H. Schaubert, D. R. Wilton, and A. W. Glisson, *A tetrahedral modeling method for electromagnetic scattering by arbitrarily shaped inhomogeneous dielectric bodies*, IEEE Trans. on Antennas and Propagation, vol. 32, pp. 77–85, 1984.